ORIGINAL ARTICLE

lajss.org© Latin American Journal of Solids and Structures

www.lajss.org

Preformed Fragment Velocity Distribution of Elliptical Cross-section Projectile

Ximin Deng[a], Haijun Wu[a*], Xiang Yang[a,b], Wenhui Xie[c], Fenglei Huang[a]

[a]Stake Key Laboratory of Explosion Science and Technology, Beijing Institute of Technology, Beijing 100081, China. E-mails: bitdengxm@bit.edu.cn; wuhj@bit.edu.cn; huangfl@bit.edu.cn.
[b]COMAC ShangHai Aircraft Design and Research Institute, Shanghai 201210, China. E-mail: 18810996251@163.com.
[c]Chong Qing Hongyu Precision Industry Group Co. LTD, Chongqing 402760, China. E-mail: 634629420@qq.com.

*Corresponding author

https://doi.org/10.1590/1679-78256835

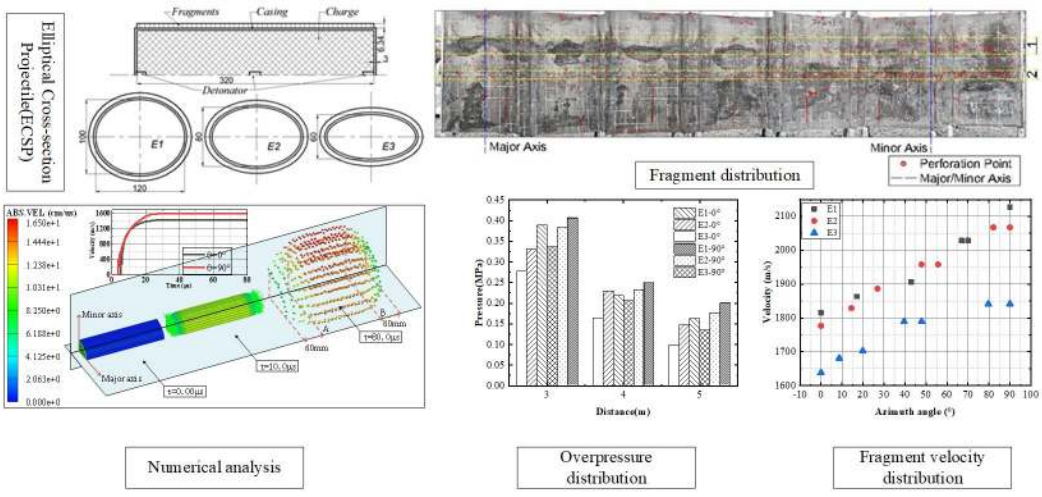
Abstract

In the field of warhead design, non-cylindrical warhead, especially elliptical cross-section warhead, has received considerable attention. In this study, the initial velocity and distribution characteristics of the preformed fragments of a columnar projectile with an elliptical cross-section were examined. To obtain the velocity distribution of the fragments in this kind of projectile, three elliptical cross-section projectiles with different geometric sizes were test based on the static detonation tests. Then, the numerical models of the elliptical cross-section projectile have been established and validated according to the experiment results. Besides, two kinds of initiation types were studied by the simulation model, and the results indicate that not only the geometric size but the initiation type do great influences on the fragment velocity distribution in the direction of the axis. An empirical model was proposed based on the fragment two-step acceleration progress, and it was in good accordance with numerical results.

Keywords

Elliptical cross-section projectile, Preformed fragment, Fragment velocity, Detonation wave, Rarefaction effect.

Graphical abstract



Received November 07, 2021. In revised form November 22, 2021. Accepted November 22, 2021. Available online November 23, 2021
https://doi.org/10.1590/1679-78256835

Latin American Journal of Solids and Structures. ISSN 1679-7825. Copyright © 2021. This is an Open Access article distributed under the terms of the Creative Commons Attribution License, which permits unrestricted use, distribution, and reproduction in any medium, provided the original work is properly cited.

Introduction

In recent years, the aerodynamic shape methodology of a high lift-to-drag ratio has been continuously applied to the design of new aircraft. Owing to the flattening of aircraft shapes, noncircular projectiles are also being developed to adapt to the internal space of aircraft. With the emergence of noncircular cross-section projectiles [1-4], the model for the fragment velocity of a cylindrical projectile is no longer applicable. Therefore, research on noncircular cross-section projectiles is particularly important. There are few studies on the fragment velocity of projectiles with noncircular cross-sections, and the characteristics and mechanisms of the detonation propagation progress of this type of projectile are still unclear. Besides, as fragment velocity is an important index to measure the effectiveness of the projectile, research in this regard is of great practical significance.

Intending to study the influence of noncircular geometry on the fragment velocity, Ding [5], Guo [6][6][7], Ning [8], and Marriott CO [9] studied the distribution of the fragment velocity of projectiles such as D-shape and prismatic projectiles. They found that during eccentric initiation, the detonation wave propagation was similar to that in a noncircular section, and the fragment velocity was no longer uniform. Ning [8] designed a prismatic casing, which the fragment velocity was investigated experimentally by high-speed photography. The results indicate that the fragment velocity was influenced by the rarefaction wave from both the axial and transverse directions. Guo [10] studied the propagation of the detonation waves in the D-shape casing. Based on the analytical study on the detonation wave propagation progress, a mathematical formula was established. According to the numerical simulation, the acceleration process of fragments in the bottom part of the D-shape casing was studied. The results indicate that the fragments were accelerated not only by the initial detonation wave but the detonation wave reflected from the arc part casing.

The detonation wave propagation process in the elliptical cross-section projectile is not clear yet. Preliminary analysis indicates that the detonation wave will reflect several times inside the casing, similar to the detonation wave propagation process in the asymmetrically initiated warhead. Therefore, the research method of asymmetrical initiation can be used for reference. Huang [11] modify the Gurney formula to predict the velocity distribution of cylindrical rings under eccentric point initiation and indicated that the projecting angle of fragments would be the same as the normal direction of cylindrical rings. Feng [12], Song [13] proposed a fragment velocity calculation model for eccentric initiation. Lv [14] analyzed the fragment velocity field and the destiny distribution of the eccentric detonation aimed warhead and found that the fragments velocity came to the maximum in the opposite direction on detonation point where the enhancement came to 10.45%, while the destiny fell for about 5.12% comparing with the center initiation. Based on the modified Gurney formula, Waggener [15] predicted the fragment velocity in the directional zone of single-side eccentric initiation, which has a sizeable relative error in the non-directional zone. Li [16-18] solved the fragment velocity near the detonation point and opposite side during eccentric two-line initiation by using the theory of the one-dimensional detonation drive.

The studies mentioned above have made a great deal of analysis on noncircular section warheads and eccentric initiation warheads. However, the fragment velocity will be affected by the rarefaction wave from both the axial and transverse directions, and the fragment velocity near the end face will be significantly reduced. Therefore, the fragment velocity distribution along the projectile axis is also of great research value when the projectile is affected by the rarefaction wave from the end face. Regarding the distribution of the velocity along the axis of the projectile, references [19-30] discuss the influence of the rarefaction waves at both ends of the projectile on the axial movement of the fragments. Zulkoski [19] proposed a modified model in exponential form to describe the influence of rarefaction waves at both ends on fragment velocity. According to this model, Huang [27] established a correction formula to represent the influence of rarefaction waves, which could predict the axial distribution of the fragment velocity. Grisaro [30] designed a series of numerical models to verify the accuracy of the fragmentation velocity distribution in the cylindrical casing and analyzed the merits and demerits of different simulation methods. The results indicated that the velocity distribution could be described by a shape function that depends on the aspect ratio.

The fragment velocity distribution of various noncircular cross-section projectiles has been studied previously. However, the fragment response and detonation acceleration mechanism in an elliptical cross-section projectile (ECSP) remain unclear. In this study, the ECSP with preformed fragments was examined as follows. This paper begins with the experimental study on the fragment velocity of the ECSP, and the velocity distribution of the fragment was analyzed. It was observed that the fragment velocity and overpressure were surprisingly inconsistent with instinct. Then, the numerical models of the ECSP had been established based on the SPH and validated with experimental data. Both the geometric size and the initiation type were studied, and the results show that those factors greatly influence the fragment velocity. Then, based on the study of the validated 2D numerical models and detonation wave propagation process, the result implied that the reflection of the detonation wave leads to the inconsistent mentioned above. Furthermore, an empirical model with good accuracy was established to estimate the fragment velocity distribution of the ECSP. The research findings can pave the way for further studies on noncircular cross-section projectile and engineering applications such as warhead design.

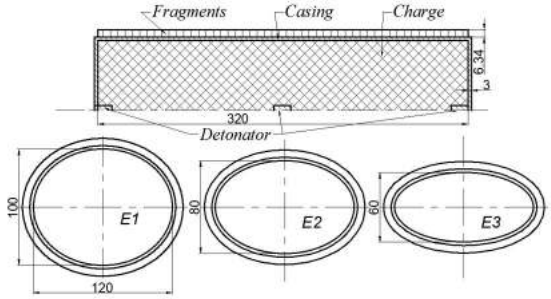
Experiment

Problem description

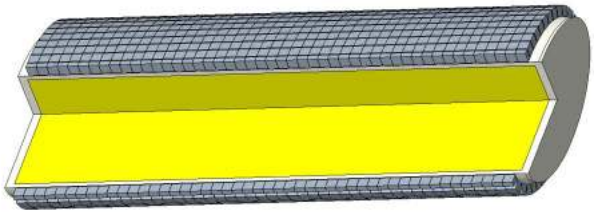
The geometry of the ECSP is different from the common warhead, and the fragment velocity distribution and projection may have a particular form. Based on the research results of the asymmetrically initiated warhead [11], the fragment project direction of ECSP may be the same as the normal direction of the ellipse. Based on the Gurney formula, the fragment velocity is related to the ratio of the mass of a single fragment to the mass of the charge, so it can be considered that the fragment velocity may decrease gradually from the major axis direction to the minor axis direction. In order to verify the conjecture mentioned above and find out the fragment velocity and distribution of the ECSP, three specimens with different ratios of major axis and minor axis were designed, and explosion experiments have been performed.

Experimental methodology

Three specimens were designed for explosion experiments to study the distribution of overpressure and fragment velocity with the elliptical cross-section, as shown in Figure 1. The lengths of the major axes were 120 mm, and the influence of the elliptical cross-section on the fragment distribution was based on changing the length of the minor axis. The charge was composed of Composition B (64/36 RDX/TNT, ρ=1.71 g / cm^3), the casing was made of ASTM 2024 aluminum, and the preformed fragments were made of ASTM 4340 steel. The thickness of the casing and end cover was 3 mm and 5 mm, respectively. The lengths of the fragments, specimens, and major axes of the elliptical cross-section were 6.34, 320, and 120 mm, respectively. The centerline initiation was difficult to achieve in the experiment. In order to achieve a similar effect, the initiating mode was set as three-point initiation, and the detonation points were the two endpoints and the midpoint of the charge. In order to ensure the uniformity of explosive mass, casting explosive was adopted. The corresponding parameters are listed in Table 1.



a) Schematic diagram of specimens.



b) 3D model



c) The photo of the specimens.

Table 1. The parameters of the specimens.

No.	Length of minor axis (mm)	Mass of charge (kg)	Mass of specimen (kg)
E1	100	4.5	10.2
E2	80	3.6	9.0
E3	60	2.6	7.7

The setup of the experiment is shown in Figure 2. To record the fragment distribution, fragment velocity, and overpressure, seven steel plates were distributed at 5 m from the detonation center. Considering that the fragment distribution in the direction of the minor axis was denser than that of the major axis, the angle between the end face of

the plates and the minor axis was 20°, to collect more information about the fragments on the plates. Five net plates were arranged at intervals of 22.5° and 6 m and 8 m from the detonation center to measure the velocity of the fragments. The overpressure measuring equipment was arranged 3–5 m away from the detonation center in the major and minor axis directions.

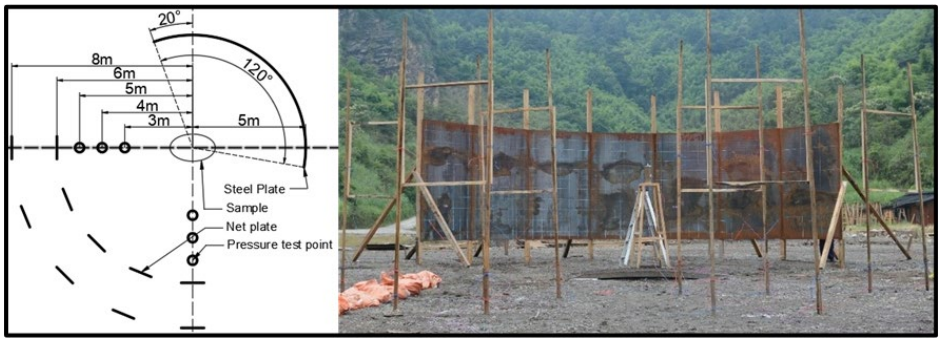


Figure 2. The schematic diagram of experimental setup.

Experimental results analysis

In the discussion of the experimental results, the major axis and minor axis of the ellipse are defined as *x*-axis and *y*-axis, respectively; the origin of coordinates is located at the center of the ellipse. All analysis and discussion are confined to the first quadrant. In order to simplify the expression, symbols and abbreviations that frequently appear in the whole text are defined as follows:

θ—azimuth angle. The angle is formed by the line between the fragments, the detonation center, and the major axis. In the first quadrant, the major and minor axes are 0° and 90°, respectively.

η—projection angle. The angle between the direction of the fragment velocity and the *x* axis.

λ—ratio of the minor axis to the major axis of the ellipse.

x_a—ratio of the axial position of the fragment to the specimen length.

v_a—fragment velocity of the single-side initiation projectile.

v_r—fragment velocity in the middle section of the centerline initiation projectile.

IntP—the integral of pressure over time.

ECSP—elliptical cross-section projectile.

The fragment velocity of ECSP is not uniformly distributed circumferentially, so the velocity measured by the net plates cannot represent the fragment velocity at the corresponding azimuth angle. Referring to the research results of Huang [11], it is assumed that the motion of the fragment is the same as the normal direction of the elliptic arc at the location of the fragment, as shown in Figure 3.

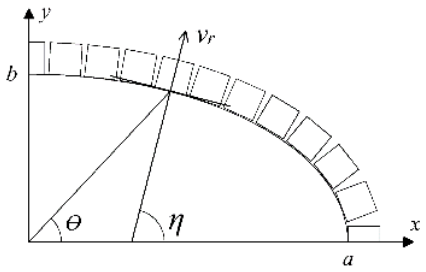


Figure 3. The schematic diagram of projection angle.

Combined with the elliptic equation, the fragment projection angle η can be expressed as

$$\eta = \arctan\left(\frac{a^2}{b^2}\tan(\theta)\right) \tag{1}$$

Where, *a* and *b* are the semi-major axis and semi-minor axis of the ellipse respectively.

The projection angle of each specimen was obtained using Eq.(1), and the trace line of the fragments was drawn, as shown in Figure 4. The first, second, and third quadrants correspond to E3, E2, and E1 in the experiments, respectively. The fourth quadrant is the locally enlarged view of the specimens. The blue and red dashed lines represent the trace lines of fragments calculated by Eq.(1) and numerical simulation, respectively, and the acquisition method of the latter will be discussed in Section 3.1.3.

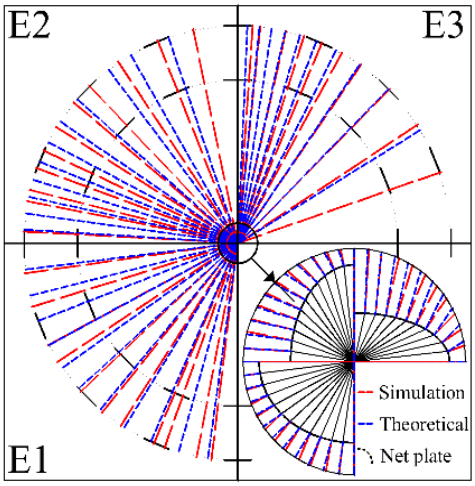


Figure 4. The schematic diagram of fragment trace line.

It can be seen from Figure 4 that the direction of ECSP fragment movement is not uniformly distributed, and the fragment distribution shows the phenomenon of focusing, that is, the fragment distribution at the minor axis direction is dense, while the number of fragments at the major axis direction is sparse, and the number of fragments increases with θ increasing. In addition, the fragment focus also increases with the decrease of λ. By comparing the theoretical and the simulated values in Figure 4, it can be seen that the motion direction of the fragment at $\theta = 0^{\circ}$ or $\theta = 90^{\circ}$ is completely consistent with the normal direction of the position of the fragment on the ellipse. The movement direction of the fragment near the minor axis is close to the normal direction of the ellipse, while the fragment near the major axis has a large deviation from the normal direction of the ellipse, and the deviation is more prominent with the decrease of λ.

Table 2. Trigger time of net plates and local velocity of fragment

Experiments units	E1			E2			E3		
	6m	8m	v_t	6m	8m	v_t	6m	8m	v_t
	Time/μs		m/s	Time/μs		m/s	Time/μs		m/s
0°	3.735	5.384	1546.207	3.816	5.499	1513.606	4.222	5.846	1394.717
22.5°	3.720	5.125	1586.951	3.759	5.266	1557.755	4.138	5.732	1422.828
45°	3.622	5.028	1623.777	3.605	5.166	1606.488	4.092	5.578	1450.182
67.5°	3.446	4.668	1727.333	3.564	4.843	1667.701	3.925	5.266	1523.85
90°	3.247	4.508	1811.432	3.335	4.644	1761.002	3.778	5.168	1568.036

Table 2 gives the trigger time of each net plates and the fragment velocity at 7 m. According to Eq.(2), the initial velocity of fragments can be calculated as follows:

$$v = v_t \exp(-\frac{R}{Hm_p^{1/3}}) \tag{2}$$

Here, v_t and v are the local velocity and initial velocity of the fragment respectively, R and H are the movement distance and attenuation coefficient respectively, and m_p is the mass of fragment. For the cube fragment, $H = 346m/kg^{1/3}$.

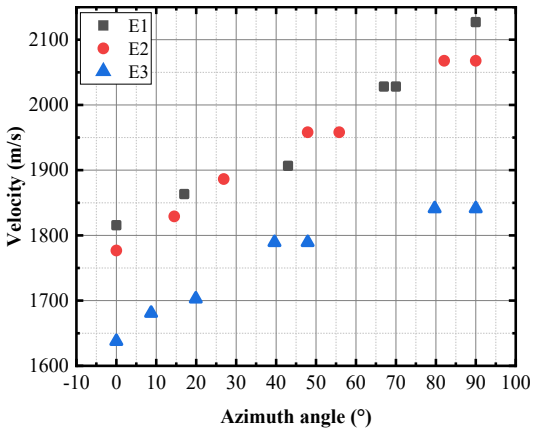
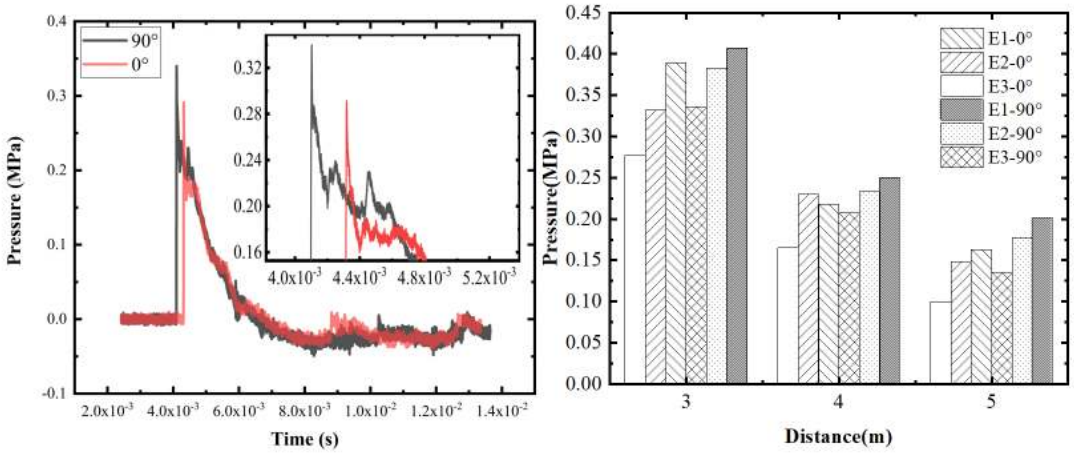


Figure 5. The $v-\theta$ curves of experiments.

In order to obtain accurate fragment velocity distribution, the intersection of the trace line and net plates was comprehensively considered to obtain the variation of fragment velocity with θ in each experiment, as shown in Figure 5. As can be seen from Figure 4, there are two fragments passing through the same net plate. Since it was impossible to identify which fragment reached the net plate earlier, the velocity of the two fragments was assumed to be the same, resulting in the situation of more than 5 data points in Figure 5.

As shown in Figure 5, the relationship between the fragment velocity and θ is completely different from the conjecture in section 2.1, which is quite confusing. The fragment velocity increases as θ increases, and the velocity in the minor axis direction is higher than that in the major axis direction. According to the derivation of the Gurney formula, the fragment velocity is correlated with the mass of charge below the fragment. Fragments along the major axis direction correspond to more explosives than those along the minor axis, so the fragment velocity along the major axis should be higher. However, considering the geometry of the elliptical casing will make the detonation wave oblique reflection and detonation wave converge in partial regions, which leads to the uneven velocity distribution of fragments. At the beginning of initiation, the fragment velocity along the major axis was higher than that along the minor axis. With the reflection and superposition of the detonation wave on the ellipse casing, the fragments in the minor axis direction were accelerated by the detonation wave again, which makes its velocity exceed that of the major axis.



a) The pressure-time curves of E3 at 3 m. b) The maximum pressure of each specimens at 3, 4, and 5 m.

Figure 6. The overpressure distribution in E1-E3.

Figure 6 shows the distribution of overpressure in the major ($\theta = 0^{\circ}$) and the minor axis ($\theta = 90^{\circ}$) at distances of 3–5 m from the detonation center. The overpressure distribution like the velocity distribution — the overpressure in the minor axis direction is higher than that of the major axis.

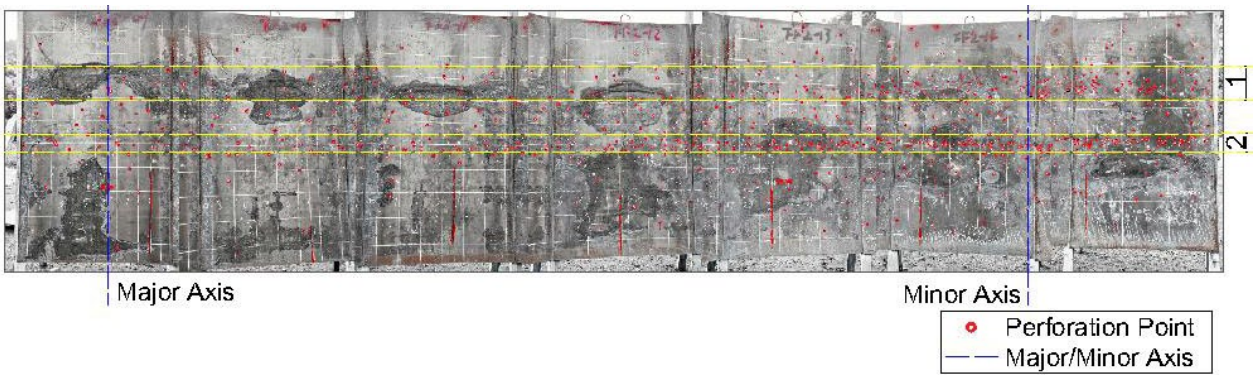


Figure 7. The schematic diagram of fragment distribution (E3).

Figure 7 depicts the fragment distribution in E3, in which the red dots represent the holes in the plate after fragment penetration; the two blue vertical lines correspond to the major and minor axes of the specimen, respectively; the two pairs of yellow lines indicate the area where fragments were concentrated. The dark areas on the plate are rust, which is unrelated to the explosive damage of the specimen. It can be compared with the plate in Figure 2 (before the experiment).

Table 3. The distribution of fragments.

Experiments		-20°–-5°	-5°–10°	10°–25°	25°–40°	40°–55°	55°–70°	70°–85°	85°–100°	Total
E1	Number of fragments	74	68	76	89	92	92	89	102	682
	Percentage (%)	10.9	10	11.1	13	13.5	13.5	13	15	
E2	Number of fragments	54	52	60	70	89	105	123	135	688
	Percentage (%)	7.8	7.6	8.7	10.2	12.9	15.3	17.9	19.6	
E3	Number of fragments	31	31	42	52	89	124	180	156	705
	Percentage (%)	4.4	4.4	6	7.4	12.6	17.6	25.5	22.1	

As shown in Table 3, the fragment distribution of the ECSP was significantly different from that of the circular cross-section projectile. The fragment distribution was sparser near the major axis, denser near the minor axis, and the perforation density gradually increased from the major axis to the minor axis, showing a focusing phenomenon toward the minor axis. For example, in E3, the fragments near the major axis accounted for only 8.8% of the total fragments, while the minor axis direction accounted for 47.6%. As the specimen detonates at three points on the axis, the distribution of fragments along the axial direction was stratified. Two obvious fragment bands—numbered 1 and 2—were found on the plate, as shown in Figure 7.

The hypothesis of fragment motion trace in Section 2.2 is verified by the statistics of fragment distribution mentioned above. The direction of the fragment motion coincides with the normal cross-sectional position of the projectile—that is, the direction of the fragment motion is related to the shape of the casing. However, it should be noted that there is a large deviation between the movement direction of fragments near the major axis and the normal direction of the casing.

The experimental results indicate that ECSP has the function of directional damage. On the one hand, the fragment velocity along the minor axis direction is higher than that along the major axis. On the other hand, fragments were densely distributed along the minor axis of the ellipse. Combined with the above two characteristics, ECSP will gather more high-velocity fragments in the minor axis direction after detonation, and it has the function of efficient directional damage.

Numerical analysis

In Section 2.3, the mechanism of the fragment velocity in the minor axis is higher than that in the major axis was preliminarily analyzed. It is pointed out that the detonation wave impacts the fragments along the minor axis several times after reflection and superposition, which leads to the increase of the fragment velocity in the direction of the minor axis. In this section, a series of numerical simulation models were established to verify the correctness of the above conclusion. Further, the relationship between λ and fragment velocity and the distribution of fragment velocity along the axis were studied.

Numerical simulation method

A series of simulation models were established in AUTODYN to solve the above problems, and the propagation process of the detonation wave in the elliptical casing and the fragment velocity distribution were analyzed. In the process of the explosion and detonation wave accelerate fragments, high strain rate, large deformation, casing fragmentation, and the effect of detonation wave on the structure make the simulation calculation more difficult. Commonly used methods, such as Lagrange methods, Euler methods, and Arbitrary Lagrange Euler (ALE) methods, are no longer applicable. In recent years, the Smoothed Particle Hydrodynamics (SPH) methods are often used to study explosion and fragmentation. Therefore, in this study, the SPH method was used to simulate the explosion and fragment velocity of ECSP.

Numerical simulation model

The simulation method of fragment velocity in the explosion process has been mature, and the parameters such as structure parameters, material models, and particle size can be determined. The materials in the numerical simulation were consistent with those in the experiments. The charge was set as Composition B, the casing was set as ASTM 2024 aluminum, and the preformed fragments were set as ASTM 4340 steel. Composition B is a common explosive whose state after explosion can be characterized by the JWL equation. The material parameters of Composition B can be obtained from the AUTODYN material library[31]. ASTM 2024 aluminum burns under the acceleration of detonation waves. During the experiments in Section 2, only a small number of casing fragments were found on the steel plates, so it was considered that the Casing had been totally disintegrated during the explosion. Johnson-Cook constitutive model can describe its dynamic mechanical property. The material parameters of ASTM 2024 aluminum can be obtained from the references [32] and listed in Table 4.

Table 4. The parameters of material of casing.

$\rho_0\,(\mathrm{kg/m^3})$	v	$E(\mathrm{GPa})$	$T_r(K)$	$T_m(K)$	$A(\mathrm{MPa})$	$B(\mathrm{MPa})$	n
2780	0.33	73.083	300	775	369	684	0.73
C	m	$C_p\,(\mathrm{J\cdot kg^{-1}\cdot K^{-1}})$	D_1	D_2	D_3	D_4	D_5
0.0083	1.7	875	0.13	0.13	-1.5	0.011	0.0

Fragments scattered in the soil were collected after the experiments, and the structure of the fragments remained intact. So, it can be considered that the fragments were undamaged during the acceleration of the explosive. That is, the fragments were set as non-failure in the simulation calculation process. Johnson-Cook constitutive model can describe its dynamic mechanical property, and the material parameters of ASTM 4340 steel can also be obtained from the AUTODYN material library[31].

In the simulation model, the explosive was set as SPH particles, and the casing and fragments were set as Lagrange elements. Considering the symmetry of the specimen, a 1/4 numerical model was established, and it is shown in Figure 8. Guo[7] indicated that the SPH model would be accurate enough to simulate the axial rarefaction waves effects and the propagation of detonation waves in the casing when the radius of the particles was smaller than 0.4 mm. In this case, the particle radius was set as 0.4 mm. After several simulation calculations and a comparison of the velocity distribution of fragments in the experiments, the grid size of the casing and fragments was set as 1 mm.

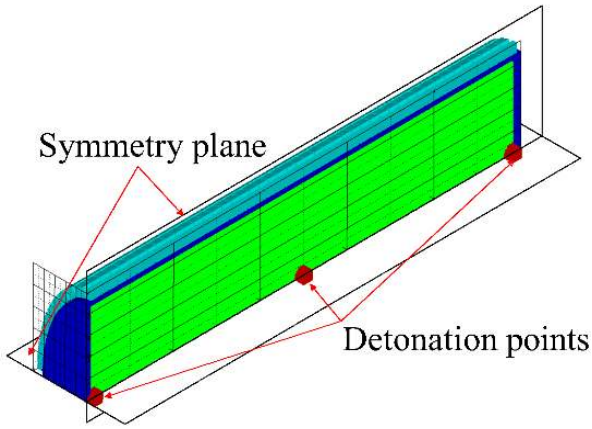


Figure 8. The schematic diagram of the 1/4 numerical model.

Simulation model validation

Simulation models corresponding to experimental specimens in Section 2.2 were established to verify the effectiveness, as shown in Figure 8. The detonation mode was a three-point initiation, and the detonation points were the two endpoints and the midpoint of the charge.

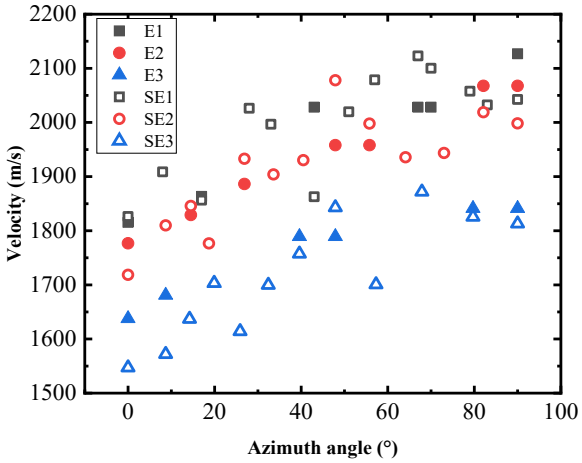


Figure 9. Comparison between experimental and simulation results.

Comparison of numerical simulation and experimental results are shown in Figure 9. Among them, E1, E2 and E3 represent the experimental results, and SE1, SE2 and SE3 are the simulation results of corresponding samples, respectively. As shown from the figure, the simulation results of $\theta = 90^{\circ}$ are basically the same as the experiment, and the relative error is less than 3%. When $\theta = 0^{\circ}$, the relative error of E3 and SE3 is 5%, while the relative error of the other two groups of data is small. When $0^{\circ} < \theta < 90^{\circ}$, the simulation results are basically consistent with the experiments, and the maximum relative error of E1 is less than 7.8%, and the maximum relative error of E2 and E3 is less than 6%. The assembly process of fragments mainly causes the maximum relative error of individual data points. During the assembly of fragments, fragments were poured into the gap between the casing and the tooling, which cannot be arranged according to the designed position. On the other hand, there are some deviations in calculating the fragment velocity in the experiment by the method of the intersection of the fragments trace line and the net plate. Except for a small number of data points with deviation, the other data agree with the experiment. Therefore, it can be considered that the numerical model is accurate enough to simulate the fragment velocity of ECSP.

Analysis of the fragment trace line

In Section 2.3, the method of intersecting the fragment trace line with the net plates was proposed to obtain the fragment velocity at different azimuth angles. In this section, the method of acquiring fragment trace lines was introduced, and the fragment distribution of ECSP was analyzed.

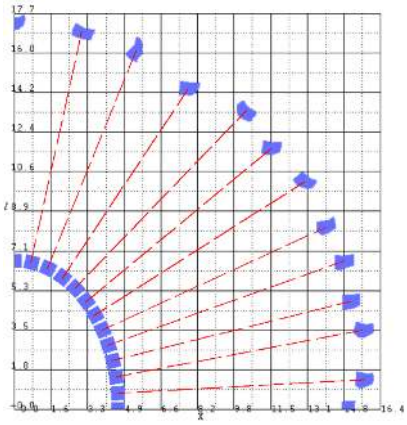
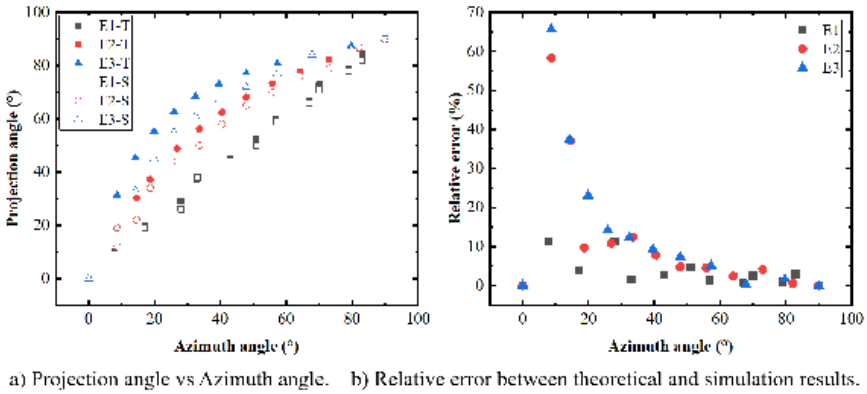


Figure 10. The schematic diagram of the fragment trace line (E2).

The spatial distribution of fragments before initiation and during movement was intercepted and placed in the same coordinate system according to the same proportional coefficient. The centroid of the corresponding fragments was connected, as shown in the red dotted line in Figure 10. The included angle between the red dotted line and the direction of the major axis is the projection angle.



a) Projection angle vs Azimuth angle. b) Relative error between theoretical and simulation results.

Figure 11. Projection angle: Comparison between theoretical and simulation results.

Figure 11 a) records the relationship between the theoretical and the simulation of the projection angle of the three specimens at different azimuth angles. Wherein, E1-T, E2-T and E3-T represent theoretical values of the projection angle of the three specimens respectively; E1-S, E2-S, and E3-S correspond to simulation data of the projection angle, respectively. Section 3.1.2 verifies the accuracy of the simulation model, so the simulation values of the projection angle were more reliable than the theoretical result. Therefore, the relative error between the theoretical and the simulation results was plotted based on the simulation data, as shown in Figure 11 b). As can be seen from the figure, the projection angles of the major axis and the minor axis are 0° and 90°, respectively. When the azimuth angle is greater than 45°, the relative error is less than 10%, and the relative error gradually increases with the decrease of λ. The relative error is greatest near $\theta = 10^{\circ}$. According to the above analysis, it can be considered that the motion direction of the fragment can be roughly estimated, that is, when $\theta > 45^{\circ}$, the fragment motion direction is consistent with the normal direction of the ellipse at its position.

Relationship between the fragment velocity and λ

From the experimental results shown in Figure 9 and the corresponding simulation results, it can be seen that the fragment velocity is affected by λ. It is necessary to further study the influence of λ, which significantly affects the shape of the ECSP and is the main parameter in engineering design. However, the influence of λ on the fragment velocity

distribution cannot be discussed without controlling a single variable, as both λ and the mass of charge were changing. Therefore, in this section, a series of ECSPs with the same cross-sectional area and different λ were established to analyze the fragment velocity.

Numerical models establishment

Seven ECSPs with different λ were designed on the basis of ensuring that the weight of the charge and fragments remain unchanged, as shown in Table 5. As the specimen detonates at three points on the axis, the distribution of fragments along the axial direction was stratified. In order to avoid the stratification mentioned above, the detonation mode was set as centerline initiation.

Table 5. The parameters of the additional model.

No.	Length of major axis (mm)	Length of minor axis (mm)	λ	Detonation mode
S1	60.00	60.00	1	
S2	63.25	56.92	0.9	
S3	67.08	53.67	0.8	
S4	71.71	50.2	0.7	Centerline initiation
S5	77.46	46.48	0.6	
S6	84.85	42.43	0.5	
S7	94.87	37.95	0.4	

The structure of the additional models was similar to the specimens in Figure 1. The charge was set as Composition B; the casing and end cover were made of ASTM 2024 aluminum with a thickness of 2 mm; the fragments were made of ASTM 4340 steel with a size of 4 mm. The 1/4 symmetry was still used to build the simulation model, and the mesh size and material constitutive model were the same as the settings in section 3.1.1. When detonating at one end, the maximum propagation distance of the rarefaction wave generated at the initiating end and the non-initiating end is 2R and R, respectively, where R is the maximum radius of the charge[29]. This conclusion indicates that no rarefaction wave influence except for the above area, so the length of charge was set as 200 mm.

Numerical results analysis

The numerical results of the elliptical cross-section projectile with different λ were obtained based on the numerical models mentioned above.

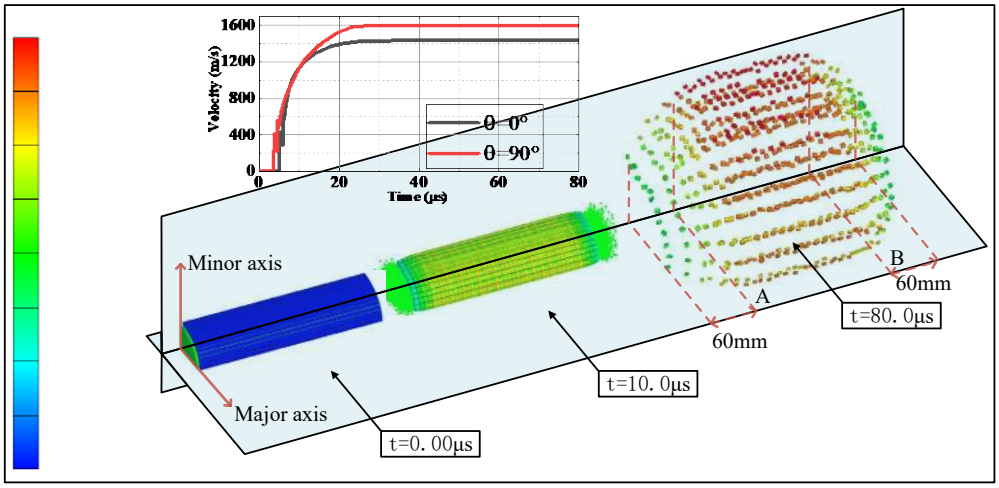


Figure 12. The schematic diagram of the fragment acceleration progress (S4).

Detonation waves in a similar process accelerated fragments in S1-S7, so only S4 was analyzed. The fragment acceleration progress is shown in Figure 12. The fragment velocity at both ends of the casing is significantly lower than

that at the middle part of the casing due to the effect of the rarefaction waves at the end faces. At about 60 mm from the end face of the casing (region AB is shown in Figure 12), the fragment velocity no longer changes with the change of the axial position, and the fragments with higher velocity were significantly concentrated in the minor axial direction. It indicates that the distribution of high-velocity fragments still shows the phenomenon of focusing in the minor axis when the centerline was detonated, consistent with the conclusion in 3.1.3. According to the velocity contour and the velocity curves of the fragments along the major and minor axes, it can be seen that the fragment velocity at each azimuth angle on the same section was basically the same at 10 μs, and the fragment velocity was not affected by θ. At 80 μs, the fragments had maintained a uniform velocity, and the fragment velocity in the major axis direction is lower than that in the minor axis direction at any section of the middle segment of the casing.

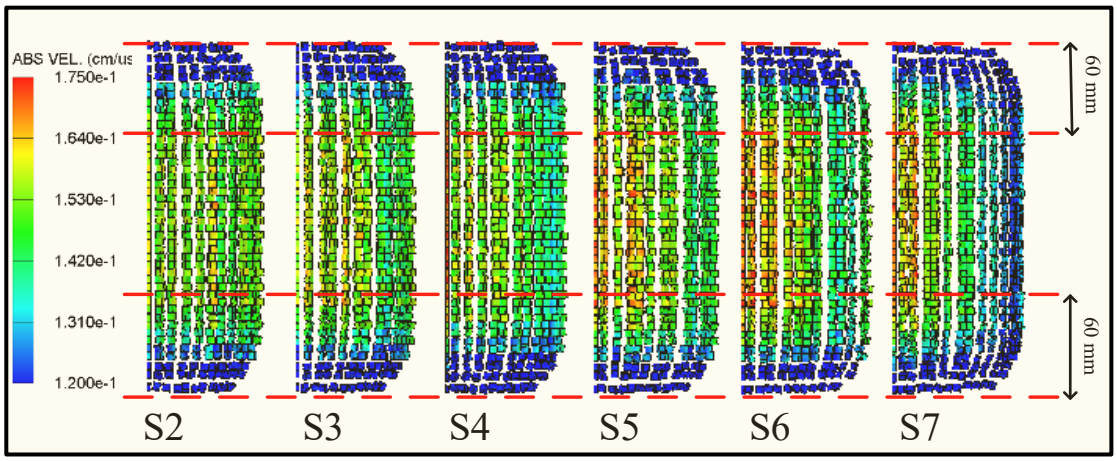


Figure 13. The schematic diagram of the fragment distribution.

Fragments in the middle segment of the casing were selected for data acquisition, and the influence of λ on fragment velocity was studied, as shown in Figure 13. In each simulation model, fragments beyond 60 mm from the end cover were not affected by the rarefaction wave, which also proves that the conclusion about the influence range of the rarefaction wave proposed in reference [29] is also applicable to ECSP (centerline initiation) in Table 5. Besides, to highlight the influence of λ on fragment velocity, the velocity range of the contour was controlled from 1200 m/s to 1750 m/s. As shown in Figure 13, the smaller the λ was, the more pronounced the difference of velocity distribution was, and the enhancement effect of fragment velocity in the minor axis was more significant.

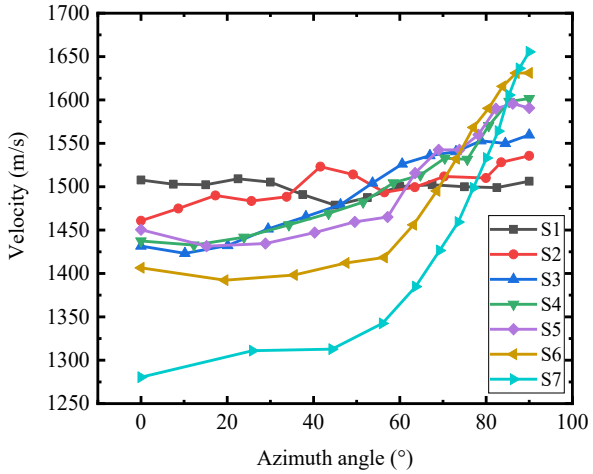


Figure 14. The $v_r - \theta$ curve of each model.

The fragment velocity at the same θ fluctuates up and down, so the maximum velocity at the same θ was averaged. The simulation data of centerline initiation in Table 5 are illustrated in Figure 14. This figure visually shows the effect of the elliptical casing on the fragment velocity. For example, the fragment velocity of S7 at $\theta = 90^{\circ}$ is 11.5% higher than that of S1, and 13.7% lower than S1 at $\theta = 0^{\circ}$.

Table 6. The main parameters of effective fragments.

	S2	S3	S4	S5	S6	S7
Count	3	4	5	7	6	5
Scattering angle δ/°	13	26	36	55	51	48
Average enhancement rate/%	2.92	3.71	5.57	5.26	7.44	7.72
Maximum enhancement rate/%	3.69	4.77	7.90	7.17	9.89	11.53
Minimum enhancement rate/%	2.30	2.38	3.27	2.12	3.23	3.28

In order to evaluate the directed damage function of ECSP more specifically, the number of fragments in S2-S7 with a velocity higher than that in S1 was counted, and the scattering angle was calculated. Among them, fragments that are 2% higher than the fragment velocity of S1 are defined as effective fragments, and the scattering angle is the angle between the effective fragments on the outer side of the minor axis and the major axis. The results are shown in Table 6. Due to the fluctuation of the velocity in the simulation, the fragment velocity of S1 was set as 1484 m/s to simplify the calculation, that is, the average fragment velocity of the mid-segment. In the second row (Count) of Table 6, the number of effective fragments on the 1/4 arc of the middle segment of the casing was counted. The number of fragments on a single circle of each model was 48; that is, the number of fragments on 1/4 arc was 13. The third row represents the average enhancement rate in effective fragment velocity relative to S1. The data listed in Table 6 shows that S5 ($\lambda = 0.6$) has the most effective fragments, and its scatter angle is the largest, and its average enhancement rate reaches 5.26%. When $\lambda\epsilon[0.3,0.6)$, with the decrease of λ, the number of effective fragments and the scattering angle decrease, but the average enhancement rate increases significantly. It can be seen that the relationship between λ and warhead damage ability is not linear. Therefore, in the design of the warhead, it is necessary to combine the characteristics of the target and select λ reasonably to achieve efficient damage.

Fragment velocity distribution of Single-side initiation

Based on the assumption that the projectile is of infinite length and is not affected by the incident angle of detonation wave, axial rarefaction wave and other factors, the relationship between λ and fragment velocity was studied in Section 3.2. However, in practical engineering design, the detonation mode is usually set as single-side initiation, and the warhead is of finite length. The fragment velocity is affected by the axial rarefaction wave and the incident angle of the detonation wave, and the fragment velocity along the axial has a specific gradient. As one of the common ways to detonate the warhead, single-side initiation plays an essential role in engineering design. This method has the advantages of simple assembly, low production cost, and no special technical requirements for the charge. After the single-side of the warhead is detonated, the detonation wave propagates from one side to the other end face. Fragments near the end face of the casing have a lower velocity when they are affected by rarefaction waves from the end faces. Therefore, it is necessary to study the projectile that detonated at one side of the charge to describe the fragment velocity distribution along the axis more accurately. The model in Section 3.3 was set as single-side initiation, and the detonation point was located at the center of the end face to analyze the influence of rarefaction waves from the end face on the fragment velocity.

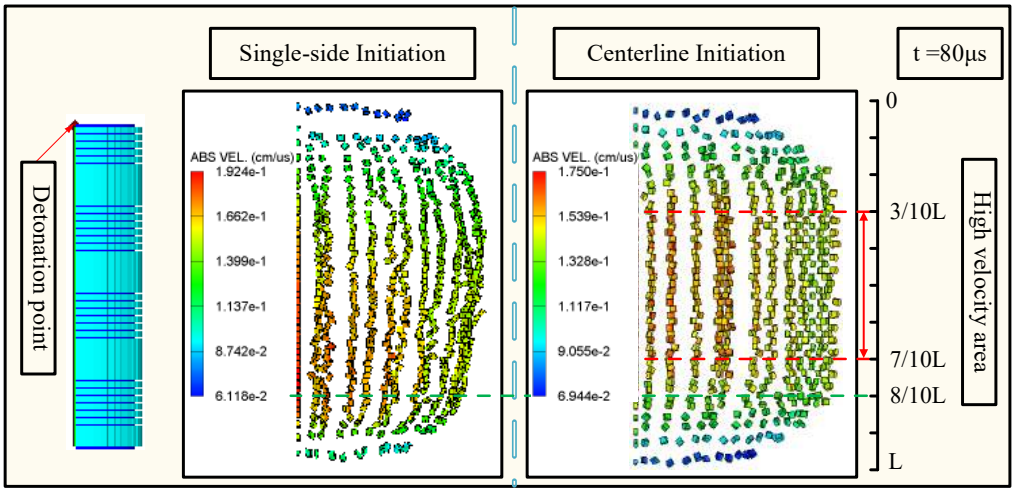


Figure 15. Fragment velocity distribution of single-side and centerline initiation (S4).

The distribution of fragment velocity along the axial of ECSP under single-side initiation is very different from that centerline initiation. Taking S4 in Figure 15 as an example, due to the end-face rarefaction wave, the fragment velocity near the end-face was lower when the single-sided was detonated, and there was a significant difference in the velocity between the initiation end and the non-initiation end. The average velocity at the initiation end was about 744.1 m/s, the average velocity at the non-initiation end was about 1050.9 m/s, and the average velocity at both ends of the casing was about 796.8 m/s when the centerline was detonated. In addition, the maximum fragment velocity of single-side initiation was located near 0.8*L*, and the centerline initiation is between 0.3*L* and 0.7*L*. It can be found that when the single-side was detonated, the fragment velocity increases gradually along the axial direction from the initiation end to 0.8*L* and then decreases. The maximum velocity of the single-side initiation is 1.1 times that of the centerline initiation.

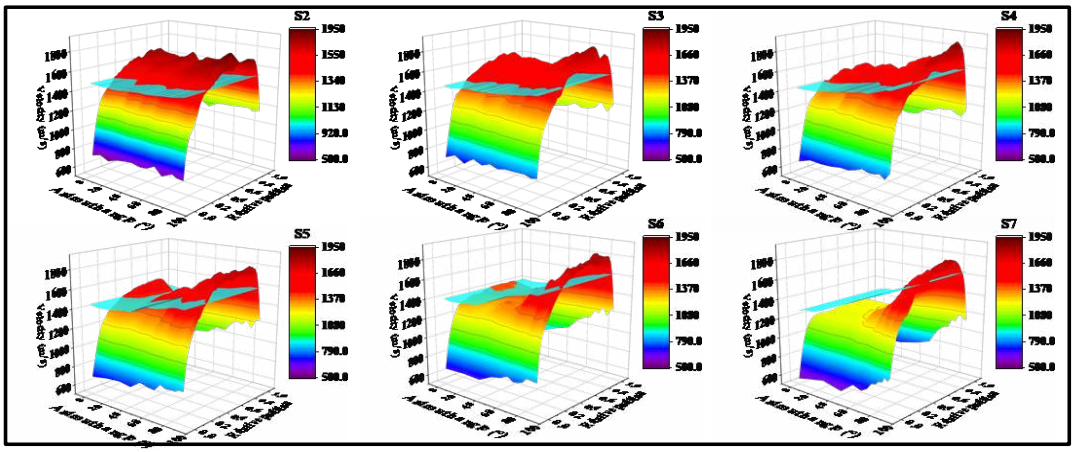
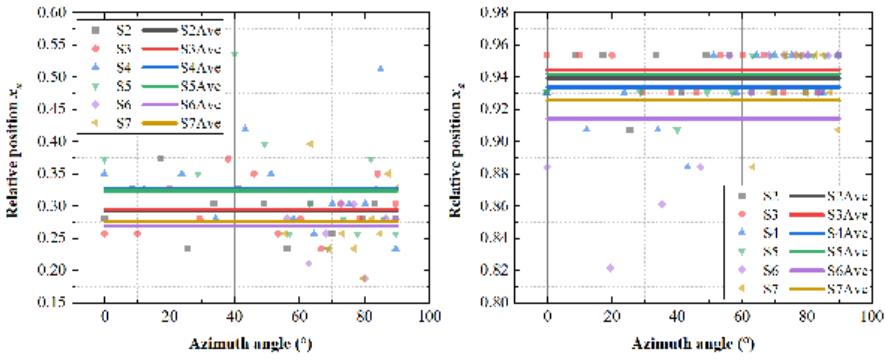


Figure 16. The $v_a - x_a - \theta$ surface of the fragments with the single-side initiation.

In Figure 16, a spatial coordinate system was constructed with v_a, θ and x_a to record the spatial distribution of fragment velocity of S2-S7 when they were detonated at a single-side endpoint. x_a represents the ratio of the axial position of the fragment to the total length of the charge, and the detonation point is set as $x_a = 0$. The distribution of fragment velocity along the axis of a single model shows that the fragment velocity at the detonation end was lower than that at the non-detonation end. The fragment velocity gradually increases from the initiation point to $x_a = 0.8L$ and then decreases rapidly. That is, fragments at the same θ reach maximum velocity at $x_a = 0.8L$. By comparing the velocity distribution of each model, it can be found that the surface was steeper in the minor axis direction and smoother in the major axis direction with the decrease of λ. For example, in S7, a larger range of smooth segments appears when $\theta = [0^\circ, 40^\circ]$, and a larger slope of convex segments appear when $\theta = (40^\circ, 90^\circ]$. The above analysis shows that the velocity in the minor axis direction increases more obviously with the decrease of λ, consistent with the distribution of velocity on the two-dimensional section (v_r) in Section 3.2.

Figure 16 also records the v_r corresponding to each model, represented by cyan face. When λ=0.9, the v_r surface intersects the v_a surface at a position near $x_a = 0.3L$ and $x_a = 0.9L$, which indicates that $v_r = v_a$ at its intersection. v_a was lower than v_r at the intersecting position to the two end sides, while the fragment velocity v_a was higher than v_r at the other positions. When $\lambda = 0.4$, the v_a surface in the range of $\theta < 60^\circ$ lies below the v_r surface, and only part of the v_a surface intersects the v_r surface when $\theta \geq 60^\circ$. In the other models, the intersection position of v_a surface and v_r surface was changed.



a) Near the initiation end b) near the non-initiation end

Figure 17. Curves of intersection position of surfaces and azimuth angle.

To make a quantitative analysis of the intersection position of the surface, Figure 17 records the relationship between intersection position and azimuth angle, where the dashed line and the solid line respectively represent the intersection position and average value and hide the data points that have not been intersected. As can be seen from the figure, the intersection positions of all models fluctuate around 0.3*L* and 0.93*L*, and the form of fluctuation is irregular to follow. Considering that the deviation between most data points and the average data is less than 10%, and the average intersection position of each model is relatively close. Therefore, it can be approximated that the intersection positions of v_r surface and v_a surface of each model are 0.297*L* and 0.933*L*, respectively.

According to the above analysis, the fragment velocity distribution of ECSP with single-side initiation can be obtained. v_a with the same θ increases gradually from the detonation point to x_a =0.8*L*, then decreases rapidly, and $v_r = v_a$ at 0.297*L* and 0.933*L*.

Mechanism analysis on the fragment velocity distribution

The conclusions in Section 3 indicate that the elliptical casing has a significant influence on the detonation acceleration process of fragments; that is, the detonation waves had multiple reflections and superposition inside the casing, which increases the fragment velocity in the minor axis direction. In order to accurately and intuitively analyze the propagation, reflection, and superposition of detonation wave inside the projectile, the propagation process of the detonation wave in the elliptical cross-section was theoretically analyzed and simulated in the two-dimensional space, and the mechanism of the axial change of fragment velocity was discussed in the three-dimensional space.

Analysis of detonation wave propagation in two-dimensional space

As mentioned above, λ affects the propagation of detonation wave inside the projectile and then affects the distribution of fragment velocity. Therefore, it is necessary to discuss the propagation of the detonation wave and analyze the propagation and reflection of the detonation wave. Assumptions were made in the theoretical analysis: the reflect angle of the detonation wave was equal to the incident angle; that is, the propagation path of the detonation wave was similar to that of the light-way [7]. Based on this assumption, the detonation wave propagation can be quantitatively analyzed simply.

A coordinate on the section of the elliptical cross-section casing is established and shown in Figure 18. In this analytical study, the focus is on the first two reflexes.

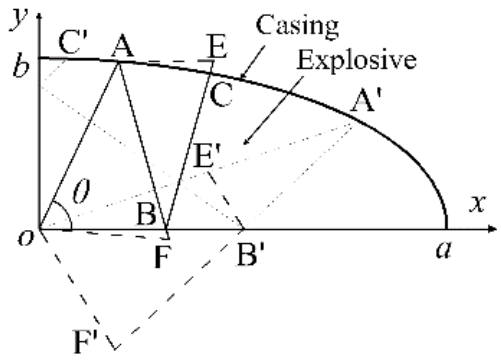


Figure 18. The schematic diagram of detonation wave reflecting progress.

When the detonation wave was reflected from the casing for the first time, the detonation wave at any position on the casing can be expressed as $A(x_A, y_A)$, which can be express as:

$$\begin{cases} x_A = \left(\dfrac{1}{a^2} + \dfrac{\tan^2(\theta)}{b^2}\right)^{-1/2} \\ y_A = \tan(\theta) \cdot \left(\dfrac{1}{a^2} + \dfrac{\tan^2(\theta)}{b^2}\right)^{-1/2} \end{cases} \tag{3}$$

The point F can be obtained on the symmetry theory and expressed as:

$$\begin{cases} x_{\mathrm{F}} = -\dfrac{\tan(\theta)}{\lambda^2} y_F \\ y_{\mathrm{F}} = \dfrac{2(y_A - \dfrac{\tan(\theta)}{\lambda^2} x_A)}{1 + \dfrac{\tan^2(\theta)}{\lambda^4}} \end{cases} \tag{4}$$

Based on the symmetry of the structure, the detonation wave has rigid wall reflection on the symmetry plane (on the *x* and *y* axes). Then, the point B can be expressed as:

$$x_B = x_A - \frac{x_F - x_A}{y_F - y_A} y_A \tag{5}$$

Also based on reflection theory, $E(x_E, y_E)$ can be expressed as:

$$\begin{cases} x_E = 2x_F - x_A \\ y_E = y_A \end{cases} \tag{6}$$

Therefore, $C(x_C, y_C)$ can be obtained as:

$$\begin{cases} y_C = \dfrac{y_E - y_B}{x_E - x_B}(x - x_B) + y_B \\ \dfrac{x_C^2}{a^2} + \dfrac{y_C^2}{b^2} = 1 \end{cases} \tag{7}$$

The same solution can be used for C'.

According to the formula mentioned above, the second impact position of reflected detonation wave with different θ can be obtained and shown in Figure 19. The coordinate position is dimensionless, so let $x_0 = x/a$, that is, $x_0 = 1$ at the major axis, and $x_0 = 0$ at the minor axis.

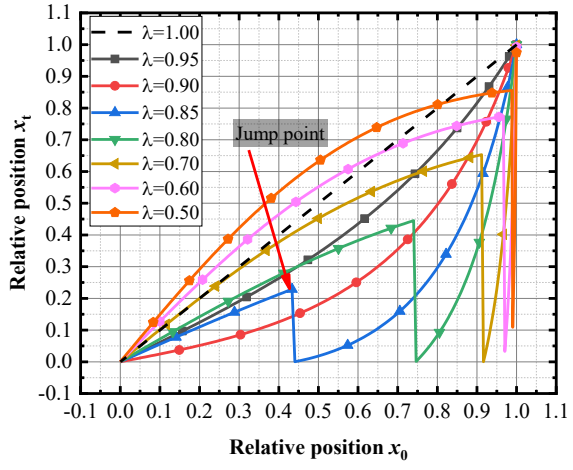


Figure 19. The $x_0 - x_t$ curves of detonation wave with different λ.

In Figure 19, each model has the same surface area and different λ. In the following analysis, only the reflection of the detonation wave on the casing and symmetry plane was considered, and the interaction of the detonation wave and pressure variation was ignored. As can be seen from the figure:

1. $\lambda = 1$, in the casing with the circular cross-section, the reflection wave on the casing was the same detonation wave as the first detonation wave. Therefore, when the circular cross-section projectile was detonated in the center, the fragment velocity at any position on the casing is basically the same.
2. When $\lambda \in [0.9,1)$, the reflected waves were concentrated in the minor axis and major axis directions, and the convergence gradually increases with the decrease of λ. When the superposition of detonation wave, pressure variation and pressure duration were not considered, the fragment velocities near the minor axis and major axis were higher, and the velocities at other positions were lower.
3. When $\lambda \in [0.5,0.9)$, the distribution of reflected wave jumps. Near the jump point, the casing in the minor axis direction will be affected by the second reflected wave. The casing near the major axis was almost unaffected by the reflected wave except for $x_0 = 1$. Taking $\lambda = 0.85$ as an example, when $x_0 \leq 0.44$, the reflected waves converge near the minor axis. When $x_0 > 0.44$, the reflected waves reconverge near the minor axis. In this kind of structure, the detonation pressure in the minor axis direction was higher than that in the major axis direction, and the pressure gradually decreases from the minor axis direction to the major axis direction, resulting in the fragment velocity near the minor axis was higher than that near the major axis direction.

Based on the above analysis, the propagation process of the detonation wave in the elliptic casing is obviously related to λ. Reflected waves gather again near the minor axis of the casing after multiple reflections, while the casing near the major axis has fewer reflected waves, resulting in high fragment velocity in the minor axis direction and low fragment velocity in the major axis direction.

The propagation of the detonation waves in the section of the elliptical casing

Numerical models establishment

The propagation of the detonation wave was quantitatively analyzed in Section 4.1. In order to verify the correctness of the analysis, the simulation calculation method was adopted in this section for a more detailed analysis. In Section 3.1 and 3.2, the 3D simulation model was calculated and analyzed, but the analysis of detonation wave propagation and reflection in the 3D model has some disadvantages and will consume much time. Besides, the 2D SPH algorithm in AUTODYN cannot construct the elliptical shape structure. Therefore, 2D ALE(Arbitrary-Lagrangian-Eulerian) algorithm was adopted in this section. Based on the geometric symmetry of the structure, the detonation wave propagation on the section far from the end was analyzed by using the planar symmetry method. 2D model can be determined as an infinite capacity for a major 3D model, but the cube fragments cannot be represented in the 2D model. For example, the fragments in Figure 20 corresponds to infinite stick fragments after conversion to the 3D model, which is not consistent with the fact. For this reason, the fragment velocity was not compared with the velocity in Section 3.2 in this section, and only the propagation of detonation wave and pressure distribution were quantitatively analyzed.

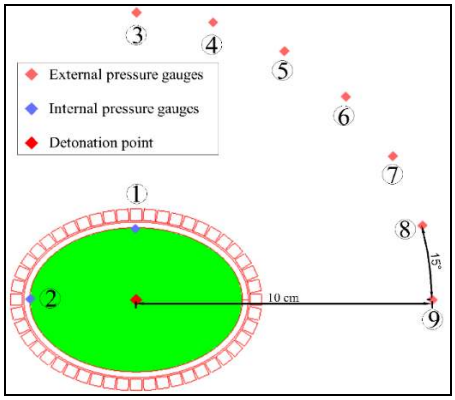


Figure 20. Schematic diagram of two-dimensional model

In order to ensure the validity of the simulation results, the grid sensitivity was verified. The calculation was carried out with a circular cross-section projectile with an explosive radius of 60 mm, a casing thickness of 2 mm, and fragments length of

4 mm. The charge was set as Composition B, the casing and the fragments were made of ASTM 2024 aluminum alloy and ASTM 4340 steel, respectively, and the constitutive models of the materials were the same as those in Section 3.1.1.

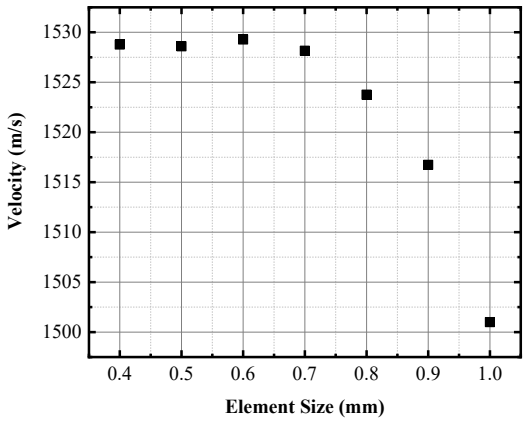


Figure 21. Fragment velocity with different element size.

It can be seen from Figure 21 that with the decrease of the mesh size, the fragment velocity gradually increases. However, when the mesh size is less than 0.7 mm, the change of the fragment velocity tends to be stable. Considering the calculation time and the accuracy of the result, the mesh size was set as 0.6 mm. In order to accurately analyze the propagation of the detonation wave and the change of fragment velocity, S4 in Section 3.2.1 was selected for calculation. Gauges were uniformly arranged on the inner wall of the casing and 10 cm away from the detonation center to obtain the detonation wave pressure changes with time at different positions, as shown in Figure 20.

Numerical results analysis

At gauge 1 and 2, the pressure on the inner wall was recorded over time, as shown in Figure 22. The solid line represents the relationship between pressure and time, while the dotted line represents the relationship between the integral of pressure over time (IntP) and time. The black curve and the red curve correspond to gauge 1 and gauge 2, respectively. To clearly display the spatial location of detonation waves, the scales of each contour are different, and the red area represents the maximum pressure at this moment.

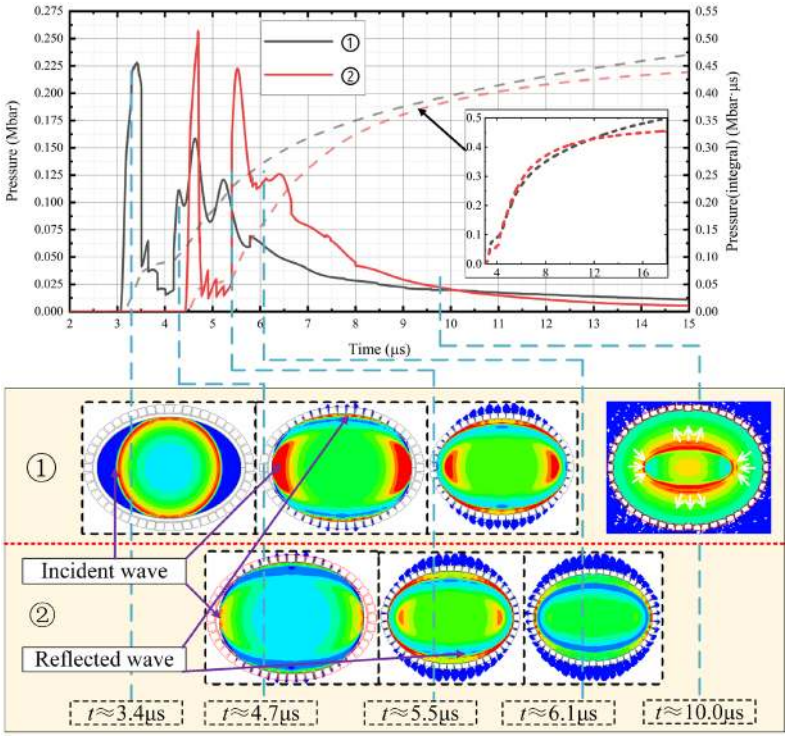


Figure 22. The detonation wave propagation process of the elliptical casing.

As shown in Figure 22, the casing in both the minor axis and the major axis experienced multiple effects of the detonation wave. To simplify the description, the unreflected/reflected detonation waves that move again towards the casing are respectively called INC/REF.

Gauge 1: At 3.07 μs, the INC passed through gauge 1 and reached its maximum pressure (0.226 Mbar) at 3.4 μs. The pressure above 0.025 Mbar lasted for 0.74 μs. There are four peaks on the pressure curve between 4.2 μs and 6.0 μs, indicating that Gauge 1 has undergone 4 REF. After 6.0 μs, the pressure at Gauge 1 decreases slowly. According to the detonation wave distribution of 10.0 μs, the detonation wave along the major axis converges towards the detonation center, while the other detonation wave still moves towards the minor axis, which indicates that there was still REF propagating along the minor axis direction. Although the pressure on the wavefront decreases gradually, the reduction of the acceleration of the fragment along the minor axis direction was slowed down.

Gauge 2:At 4.4 μs, the INC passes through Gauge 2, where the INC has interacted with the REF generated earlier, which increases the front pressure. Maximum pressure was reached at 4.69 μs (0.257 Mbar), which was 13.7% higher than the peak pressure of Gauge 1. When the casing was subjected to INC, the time when the pressure was higher than 0.025 Mbar lasts 0.306 μs, which is 58.6% lower than the duration of gauge 1. By comparing the pressure of the INC, it can be found that the peak pressure in the major axis direction was higher, but the average pressure was lower, which causes the duration of the high pressure at gauge 2 to be shorter. From 5.4 μs to 6.7 μs, a wave crest and a plateau appear on the pressure curve, indicating that gauge 2 was affected by a REF with higher pressure and multiple Refs with similar amplitudes. After 6.5 μs, the detonation wave in the major axis direction moves to the detonation center and the minor axis direction, which makes the pressure at gauge 2 drops rapidly.

To compare the relationship between IntP and time of gauge 1 and gauge 2, shift the IntP-t curve of gauge 2 to the left to 4.4 μs, as shown in Figure 22. According to the momentum theorem, IntP was positively related to the velocity, so IntP-t curve can reflect the change of velocity over time. When the two gauges were affected by INC, the pressure of gauge 1 lasts longer, which makes the velocity at this place higher than that of gauge 2. Under the influence of the first Ref, the velocity of gauge 2 rapidly increased to the same as that of gauge 1. From 6.0 μs to 6.7 μs (plateau segment), the velocity of gauge 2 exceeds that of gauge 1 due to the greater impulse. At 11.0 μs, the velocity of gauge 1 was higher than that of gauge 2 due to the convergence of the detonation wave to the minor axis direction. After that, the velocity of gauge 1 continued to increase, while the velocity of gauge 2 remained basically unchanged.

Through the analysis of the pressure change, detonation wave motion, and velocity of gauge 1 and gauge 2, combined with the conclusion of Section 4.1, it can be considered that the elliptical casing causes the detonation wave to converge in the minor axis direction after multiple reflections. In the final stage of acceleration of the detonation wave on the fragments, the impulse of the detonation wave in the minor axis direction was greater than that in the major axis, which causes the fragment velocity in the minor axis direction to be higher than the major axis.

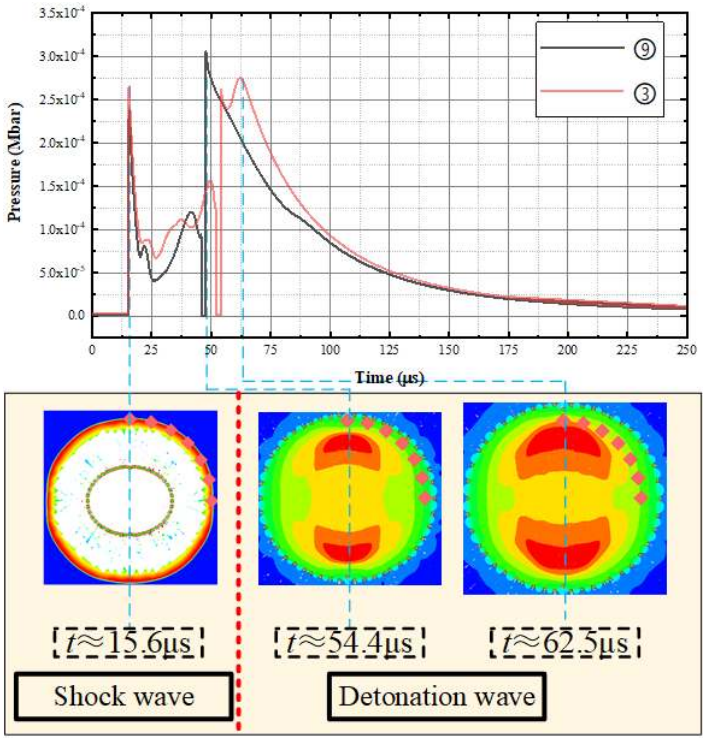


Figure 23. The pressure distribution of gauge 3 and 9.

Figure 23 records the pressure-time curves of gauge 3 and gauge 9. It can be seen from the figure that both gauges had experienced two pressure pulses. At about 15.6 μs, the shock wave moves to the gauge position before the detonation wave. The pressures of gauge 3 and gauge 9 are 26.360 Mbar and 23.751 Mbar, respectively. The shock wave was generated when the detonation wave interacts with the air. Combining the impulse generated by the first peak of the two gauges in Figure 22, it is evident that the shock wave had a more significant pressure in the major axis direction. As shown in Figure 22, at 10 μs, the detonation wave inside the casing gathers toward the center in the major axis direction and moves outward in the minor axis direction. At about 54.4 μs, the detonation wave in the minor axis direction moves to gauge 3. The pressure rise caused by the superposition of detonation waves makes the pressure at gauge 3 reach 30.528 Mbar. At about 62.5 μs, the detonation wave in the major axis direction moves to gauge 9. At this time, the pressure is 27.302 Mbar. After the two gauges were affected by the above two pressure pulses, there was no more pulse effect.

In the above discussion, gauge 3 and gauge 9 received two pressure pulses, and these two pulses were shock waves and the expanding detonation products cloud. According to the attenuation of the shock wave in the air and the expanding detonation products cloud, combined with the polytropic exponent equation of state, the pressure generated by the ECSP to the outside can be divided into two situations. First, at a place closer to the warhead, about ten times the diameter of the charge [33], the expanding detonation products cloud and the shock wave act together at this time. Second, at a place far away from the warhead, that is, more than ten times the charge diameter, the expanding detonation products cloud has attenuated to the initial pressure of the air at this time, only the effect of the shock wave exists, and the pressure in the major axis direction is lower than the minor axis direction. The shortest distance between the pressure gauge and the specimen in Section 2.3 was 3 m, which was much larger than ten times the charge diameter. Therefore, the measured data was the shock wave pressure. It can be seen that the above conclusion is consistent with the experimental results.

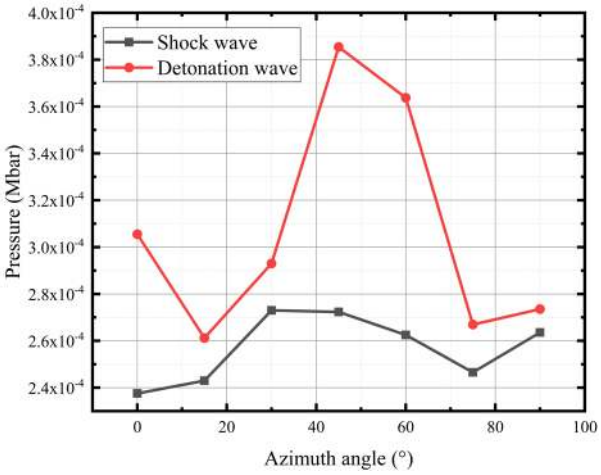


Figure 24. The pressure- θ curves of the detonation wave and the shock wave.

Gauge 4 to 8 record the pressure distribution between the major axis and the minor axis to represent a more general position. According to the previous conclusions, the first wave crest of gauges 3 to 9 is defined as the shock wave in the air, and the second wave crest is defined as the expanding detonation products cloud. Based on this definition, the pressure distribution recorded by each gauge is shown in Figure 24. It can be seen from the figure that the shock wave and the expanding detonation products cloud have a sin function relationship with θ, the maximum pressure of the shock wave is about 30°, and the maximum pressure of the expanding detonation products cloud is about 45°. This article focuses on the distribution and mechanism of fragment velocity, so the pressure distribution outside the warhead will be studied in subsequent studies.

By analyzing the propagation process of the detonation wave in the two-dimensional plane in the elliptical casing, the distribution of fragment velocity and pressure was discussed. According to the characteristics of fragment velocity changes and the detonation wave propagation in Figure 18, the process of detonation acceleration fragment can be divided into two periods. First, the plateau segment of the pressure in the direction of the major axis from the moment of initiation ends. During this period, the inner wall of the casing is affected by incident waves and multiple reflect waves. The velocity of the fragments in the direction of the minor axis is similar to that of the major axis, which means that the fragment velocity in the direction of the minor axis is less than or equal to the velocity of the fragments in the major axis. Second, after the end of the platform segment of the major axis pressure curve. During this period, the detonation wave was concentrated in the minor axis direction, the pressure in the minor axis direction was higher than the major axis, the fragments in the minor axis direction continued to accelerate, and the fragments in the major axis direction stopped

accelerating, thus exceeding the fragment velocity in the major axis direction. According to the analysis of the external pressure of the projectile, the pressure of the ECSP on the outside is divided into the shock/detonation wave combined action area and the shock wave action area. The latter is characterized by the pressure in the major axis direction lower than the minor axis direction pressure.

Analysis of fragment velocity difference with single-side initiation

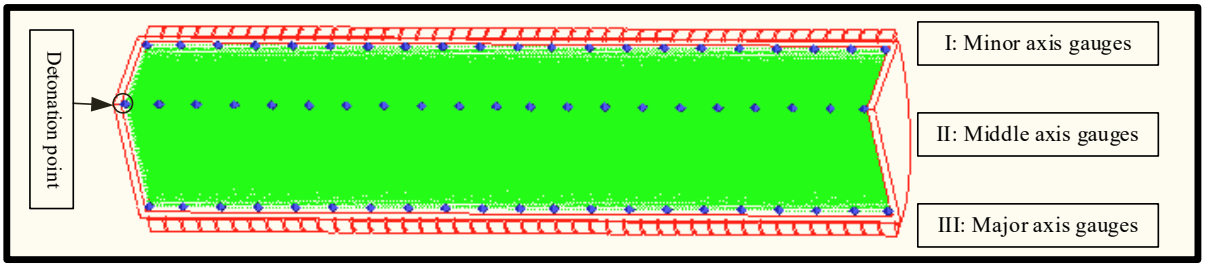


Figure 25. The schematic diagram of the gauge's distribution.

As mentioned in Section 3.3, there is a big difference between the maximum velocity of a projectile of the same structural size when it is detonated at a single-side and when it detonates at the centerline. In order to analyze the reasons for the above differences, this section takes S4 and S7 in Section 3.3 as examples for analysis. The direct factor that affects the fragment velocity is the pressure of the detonation wave, so the method in the previous section was still used to measure the pressure at a particular location inside the casing. Three gauges I-III were arranged on the minor axis, middle axis, and major axis, as shown in Figure 25.

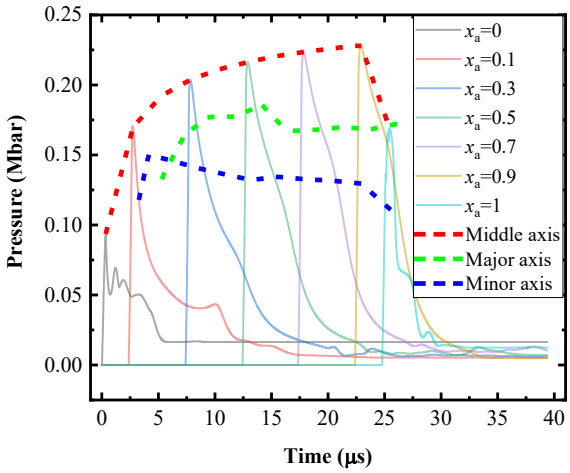


Figure 26. The pressure-time curves of the first peak (S4).

The pressure-time curve at each position is shown in Figure 26. The solid line represents the pressure-time curve of each gauge in II, and the dashed line represents the pressure corresponding to the first peak in I-III. It can be seen from the figure that the pressure on the middle axis was affected by the rarefaction wave, the pressure at the initiating end was the smallest, and the pressure at the non-initiating end was higher than the initiating end, and the maximum pressure was reached when $x_a = 0.9$. In the direction of the major axis and the minor axis, the pressure of the first peak of the major axis is higher than that of the minor axis, which is the same as the conclusion in the two-dimensional analysis. It should be noted that the fragment velocity is not only related to pressure but also related to the duration of pressure. In this regard, the pressure duration will be analyzed below.

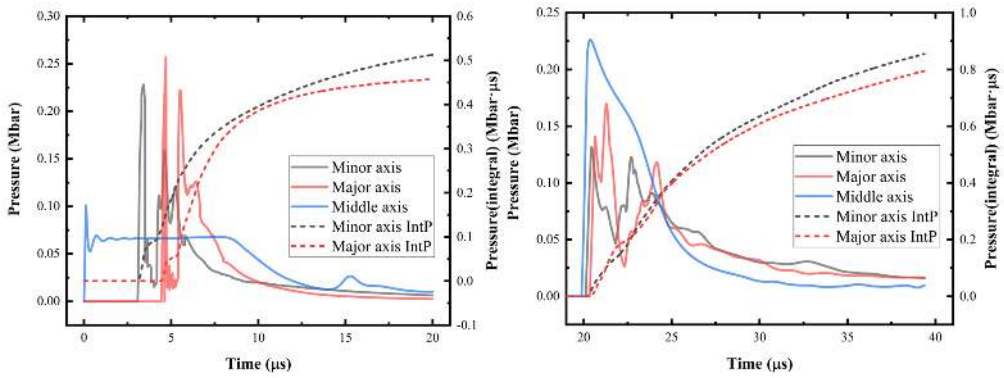


Figure 27. The pressure-time curves of two initiation type.

As shown in Figure 27, the pressure-time curves of the centerline initiation and the single-side initiation ($x_a = 0.8$) were recorded, respectively. As mentioned in Section 3.3, the fragment velocity at $x_a = 0.8$ is the largest. It can be seen from the figure that the duration of the pressure greater than 0.05 Mbar in the major axis and minor axis directions during the single-side initiation is about 5.68 μs and 6.78 μs, respectively. When the centerline was detonated, the duration of pressure greater than 0.05 Mbar in the major axis and minor axis directions was about 3.56 μs and 3.78 μs, respectively. In order to more intuitively show the relationship between pressure and time at each position and fragment velocity, IntP is also used to characterize it, as shown by the dotted line in Figure 27. Although the peak pressure in the major axis direction is higher than that in the minor axis, the IntP on the minor axis is larger; that is, the fragment velocity in the minor axis direction is higher.

The question in Section 3.3 is explained through the above analysis from the perspective of detonation wave pressure and duration: the velocity of fragments under single-side initiation is higher than that under centerline initiation. However, the reason why the v_a surface in the range of $\theta < 60^{\circ}$ is under the v_r surface has not been explained when $\lambda = 0.4$. Therefore, the detonation pressures at S4 and S7, namely $\lambda = 0.7$ and $\lambda = 0.4$, will be compared and analyzed below.

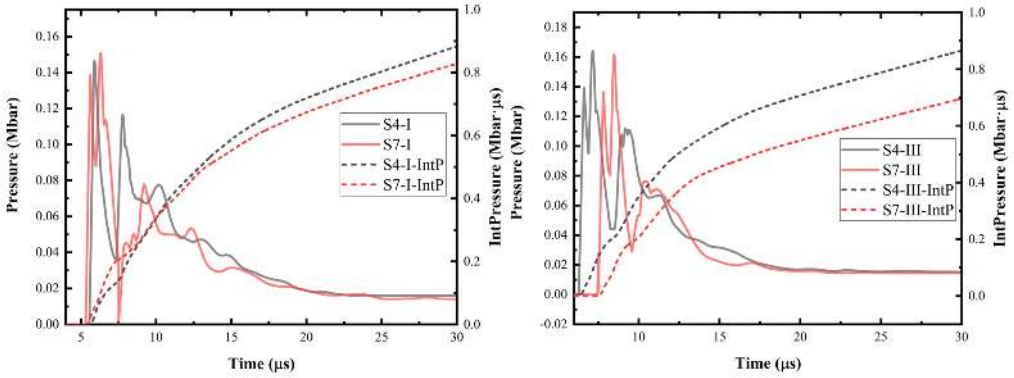


Figure 28. Comparison of the pressure between S4 and S7($x_a = 0.2$).

Figure 28 records the pressure changes when $x_a = 0.2$ along the major axis and minor axis of S4 and S7. Since S7 has a shorter minor axis and a longer major axis than S4, the two models have different durations of INC at the same position. It can be found that the pressure and duration of the INC in the major axis and minor axis directions of the two models are basically the same. The second peak, that is, the pressure of the REF, has a big difference: the pressure peaks of the INC in the major and minor axis directions of S4 were 0.112 Mbar and 0.116 Mbar, respectively; and the corresponding pressure peaks of S7 were 0.076 Mbar and 0.078 Mbar, respectively. Under the influence of INC, the IntP of S4 and S7 are basically the same, but after the effect of Ref, the IntP of the two models are different. Therefore, it can be considered that the pressure drops of the REF caused the fragment velocity near the detonation end of S7 to drop.

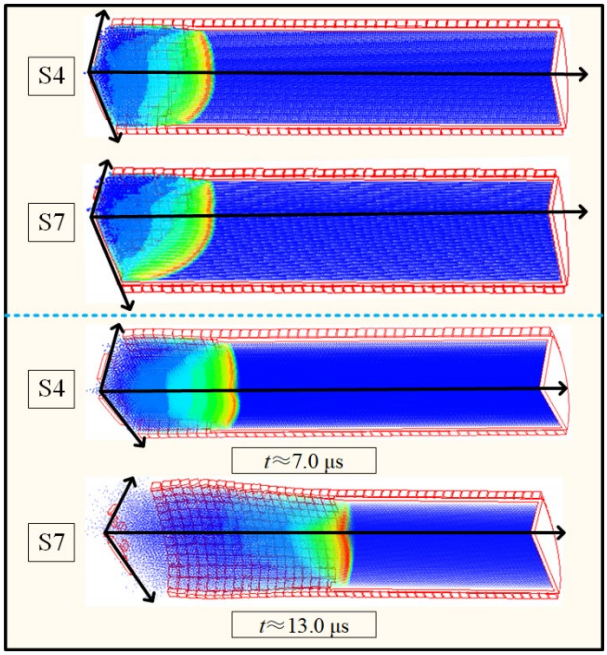


Figure 29. Comparison of detonation wave propagation process between S4 and S7.

By analyzing the detonation wave propagation trajectory of the two models, it is found that the entry of the end face rarefaction wave causes the pressure of the REF to decrease, as shown in Figure 29. Before 7.0 μs, the wave front of the detonation wave in the two models was a spherical wave. Since the detonation wave was first reflected on the casing in the minor axis direction and then reflected on the casing in the major axis direction, a wavefront with an approximate sharp-angle shape was formed and propagated from the initiating end to the non-initiating end. When the detonation wave moves to the casing in the major axis direction, the end-face rarefaction wave had entered the detonation product, causing the pressure of the REF to decrease. At 7.0 μs, the curvature of the wavefront of S4 decreases, approximately perpendicular to the inner wall of the casing, and propagates forward in the form of a plane wave. At this time, the explosive enters a stable slip detonation stage. Correspondingly, S7 enters the stable slip detonation stage at 13.0 μs. Prior to this, the detonation wave in the minor axis direction of S7 was always affected by the rarefaction wave, resulting in the pressure before entering the stable slip detonation stage lower than the major axis. For the above reasons, the v_a surface in the range of $[\lambda = 0.4, \theta < 60^{\circ}]$ was located below the v_r surface.

Through the study of the detonation wave propagation and pressure distribution when the single-side was detonated in this section, the reason for the difference in the fragment velocity distribution in Figure 16 is explained. When ECSP detonates at the single-side point, the detonation wave propagates from the initiating end to the non-initiating end. The superimposition of the reflected waves on the axis causes the pressure to increase gradually, and the fragment velocity increases along the axis. After $x_a = 0.8L$, the rarefaction wave generated at the non-initiating end reduces the pressure on the axis and reduces the fragment velocity. Affected by the elliptical casing, the detonation wave arrives at the casing in the major axis direction later than the minor axis, so that the rarefaction wave reduces the pressure on the wave front in the major axis direction. When λ is small, the rarefaction wave acts on the detonation wave in the major axis direction for a longer time, causing the explosive to form a stable slip detonation position closer to the non-initiating end, resulting in more fragment velocity v_a lower than v_r. In this regard, it is recommended that when designing an ECSP in engineering, λ should not be lower than 0.6 to avoid the influence of rarefaction waves on more fragments.

Empirical model establishment

The empirical model can provide valuable reference information in engineering design, especially for the design of fragmented warheads. At this stage, the empirical model for fragment velocity applicable to ECSP has not yet been discovered. Therefore, this section establishes an empirical model for the fragment velocity of ECSP based on the numerical simulation results and the detonation wave propagation process. According to the two periods of detonation acceleration fragments defined above, the correction term of fragment velocity can be composed of two functions. In the first period, the fragment velocities of the major and minor axis are similar, and it is approximately considered that the fragment velocity in this period has nothing to do with the azimuth angle. In the second period, when the pressure converges in the minor axis direction, the fragment velocity in this area increases, while the fragment in the major axis

direction stops accelerating. Note that S1 in Figure 14 intersects with other models, so it can be considered that the fragment velocity of ECSP is corrected based on the fragment velocity of the projectile with a circular cross-section. Through the above analysis, the fragment velocity on the ellipse section can be expressed as:

$$v_r(\lambda,\theta) = v_c\left[1+\alpha(\lambda)\cdot\beta(\lambda,\theta)\right] \tag{8}$$

Among them, v_c is the fragment velocity corresponding to the circular cross-section projectile of the same area. $\alpha(\lambda)$ represents the correction factor for the first period. $\beta(\lambda,\theta)$ represents the correction factor for the second period, and θ is converted to a radian system.

The Gurney formula can be used to calculate the fragment velocity of the circular cross-section projectile. Due to the calculated result of the Gurney formula is lower than the actual value, it needs to be multiplied by the correction factor, which is 1.146 in this article. The Gurney formula applicable to preformed fragments [33] is as follows:

$$\begin{cases} v_g = \dfrac{D}{\sqrt{5(2/\xi+1)}} \\ D = \sqrt{2(k^2-1)E} \end{cases} \tag{9}$$

where ξ is the ratio of the charge mass to the total mass of the casing and fragments, $\sqrt{2E} = 2700\ m/s$ is the Gurney constant, and *k* is the polytropic gas index, which is 2.76 [34].

Therefore, the Eq.(8) can be expressed as:

$$f(\lambda,\theta) = \frac{v_r(\lambda,\theta)}{1.146v_g}\text{-}1 = \alpha(\lambda)\cdot\beta(\lambda,\theta) \tag{10}$$

Using Eq.(10) to process the data in Figure 14, and get the relationship between $f(\lambda,\theta)$ and θ, as shown in Figure 30.

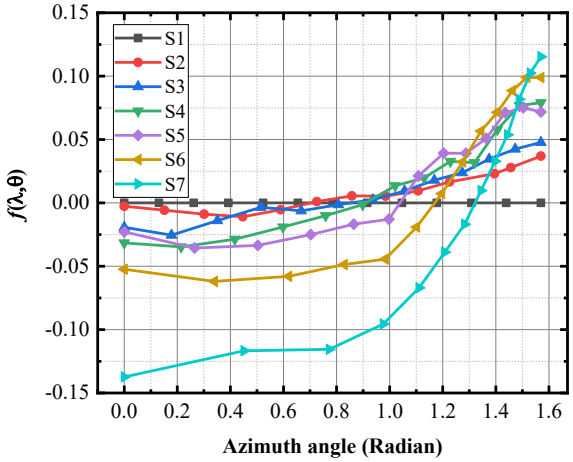


Figure 30. The $f(\lambda,\theta) - \theta$ curves of simulation data.

In the first period of fragment acceleration, the fragments in the major axis direction reach the maximum velocity, and the fragment velocity at this time is related to λ. According to $f(0,\theta)$ in Figure 30, the expression of $\alpha(\lambda)$ can be obtained:

$$\alpha(\lambda) = 1-\lambda \tag{11}$$

Substitute Eq.(11) into Eq.(10):

$$g(\lambda,\theta)=\frac{v_r(\lambda,\theta)/1.146v_g\text{ -1}}{1\text{-}\lambda}=\beta(\lambda,\theta) \tag{12}$$

Using the same method to process the data in Figure 30, the relationship between $g(\lambda,\theta)$ and θ is obtained, as shown in Figure 31.

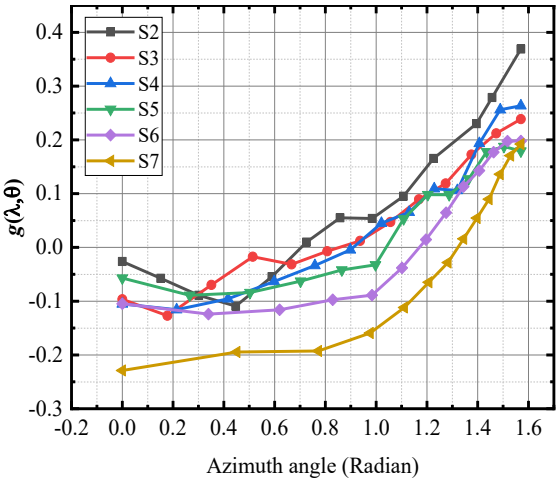


Figure 31. The $g(\lambda,\theta)-\theta$ curves of simulation data.

According to the curve of $g(\lambda,\theta)-\theta$, $\beta(\lambda,\theta)$ is defined as follows:

$$\beta(\lambda,\theta)=A+B\lambda+C\lambda^2+De^{E\theta} \tag{13}$$

Based on the 3D surface fitting method, the parameters *A*, *B*, *C*, *D* and *E* can be obtained. Through parameter fitting, Eq.(13) can be expressed as:

$$\beta(\lambda,\theta)=\text{-}0.552+0.996\lambda\text{-}0.473\lambda^2+0.018e^{2\theta} \tag{14}$$

According to the analysis mentioned above, the parameters in Eq.(8) can be determined and shown as:

$$\begin{cases} v_r(\lambda,\theta)=v_c[1+(1-\lambda)\cdot(\text{-}0.552+0.996\lambda\text{-}0.473\lambda^2+0.018e^{2\theta})] \\ v_c=1.146\sqrt{\dfrac{2(k^2-1)E}{5(2/\beta+1)}} \end{cases} \tag{15}$$

The comparison between the calculated data from Eq.(15) and the simulation data is shown in Figure 32 and Figure 33. Among them, the data points represent simulated data, and the solid lines represent calculated data. The calculated results were in good agreement with the simulation values, and the maximum relative error was less than 3.5%. Therefore, the calculation formula proposed in this paper meets the requirements of engineering applications.

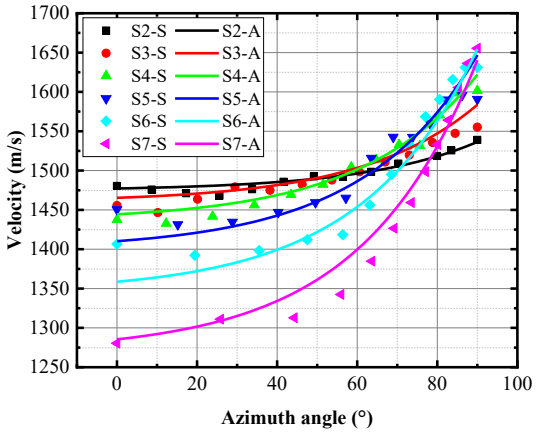


Figure 32. The comparison of analytical and simulation results.

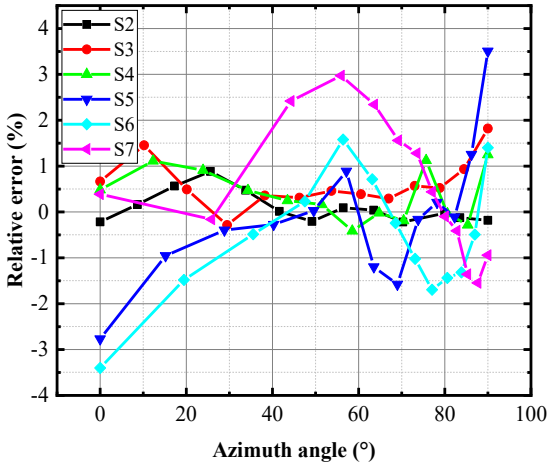


Figure 33. Relative error of analytical and simulation results.

Discussion

There are also some limitations in this study. First, there is a deviation in measuring the fragment velocity in the experiment, and the number of pressure gauges is insufficient to characterize the general position. Due to the difference between the ECSP fragment projection direction and the circular cross-section warhead, the fragment movement direction is not consistent with the line connecting the fragment location and the center of the casing, which results in the net plate data not being able to represent the fragment velocity at the corresponding position directly. The calculation of the fragment velocity in the experiment relies on the theoretical and simulation results, and there is a certain deviation between this method and the real projection of the fragment. Only the pressure gauge was arranged in the direction of the major axis and the minor axis in the experiment. Although the pressure distribution at the general position was studied in the simulation, the actual pressure of the general position still needs to be verified. Second, the detonation method in the experiments is only an approximate method of centerline initiation. The research purpose of the experiment is to analyze the fragment velocity distribution in the two-dimensional state, in which the end face rarefaction wave is not affected. It is obvious from the experiment and corresponding simulation that the fragment distribution formed by the three-point detonation and the centerline initiation is inconsistent, resulting in the empirical model that the experimental results cannot verify. Third, there is still a lack of adequate theoretical model support for the propagation of detonation waves during single-side initiation. It only analyzes the pressure distribution, pressure-time integral, and detonation wave propagation on the inner wall of the casing, but there is still a lack of understanding of its mechanism.

Based on this study, a series of valuable research can be conducted in the future. First, it is possible to design test technology suitable for the ECSP explosion experiment. For example, the introduction of the X-ray photograph technique and other technologies to observe the movement of the fragment; increase the overpressure gauge at more locations to obtain the pressure distribution of the general location. Second, study the mechanism of detonation wave propagation under single-point initiation, and establish related theoretical models, and then obtain the empirical model of the fragment velocity and the spatial distribution of fragments of the single-side initiation.

Conclusion

In conclusion, the velocity and acceleration of the fragments in ECSP have been investigated experimentally and numerically. The fragment velocity distribution in the two-dimensional state was studied, and the calculation method of projection angle was proposed. Then the influence of the ratio of the minor and major axis of the ellipse on the fragment velocity and the fragment velocity distribution at the single-side initiation were analyzed. Besides, an empirical model was established based on the mechanism of fragment velocity distribution. The following conclusion can be drawn from this study:

1. It was verified that the fragment velocity of the ECSP is different from the traditional circular cross-section projectile through static explosion experiments. The main feature is the larger fragment velocity and overpressure in the direction of the minor axis than in the direction of the major axis, showing an increasing trend from the direction of the major axis to the minor axis. With the influence of the casing shape, the fragments do not motion uniformly in the radial direction. However, it shows the focusing phenomenon of sparse fragments in the direction of the major axis and dense fragments in the minor axis. The movement direction of the fragment in the minor axis direction is consistent with the normal direction of the ellipse where it is located, which also means that the focusing phenomenon of sparse fragments in the direction of the major axis and dense fragments in the minor axis.
2. A series of simulation models had been established to discuss the influence of the ratio of the minor and major axis of the ellipse and the detonation method on the fragment velocity and analyze the influence of the detonation wave propagation, pressure distribution, and duration on the fragment velocity distribution. When ECSP detonates on the centerline, when the center point of the two-dimensional state detonates, the fragment velocity is closely related to the ratio of the minor and major axis. Combining theoretical analysis and simulation results, the fragment acceleration process was divided into two stages. In the second stage, the detonation wave gathers in the minor axis direction, causing the fragment velocity in this direction to be higher. The overpressure generated by the warhead to the outside is divided into two areas. At a position greater than ten times the charge diameter from the warhead, the shock wave pressure in the minor axis direction is greater than that in the major axis direction, and the maximum pressure is at $\theta = 45^{\circ}$. When ECSP detonates at a single-side point, the fragment velocity increases significantly along the axial direction, and the fragment velocity is the largest at a position of 0.8L from the detonation point.
3. Two correction functions were added to the Gurney formula to establish an empirical model based on the mechanism of two-stage fragment acceleration. These two correction functions correspond to the two stages of the fragment acceleration process. The empirical model can calculate the fragment velocity of ECSP at different azimuth angles during centerline initiation with a relative error of less than 3.5%, which means that the model can be effectively applied in engineering design and later analysis and research.

Acknowledgments

This work was partially sponsored by the National Natural Science Foundation of China under Grant No. 12072039.

Data Availability

The data that support the findings of this study are available from the corresponding authors upon reasonable request.

Author contributions: Conceptualization, X Deng and H Wu; Methodology, X Deng; Investigation, X Deng, H Wu, X Yang and W Xie; Writing - original draft, X Deng, and H Wu; Writing - review & editing, X Deng, H Wu and F Huang; Funding acquisition, H Wu and F Huang; Resources, H Wu and F Huang; Supervision, H Wu and F Huang.

Editor: Marcílio Alves

References

[1]. LIU Zi-hao, WU Hai-jun, GAO Xu-dong, PI Ai-guo, HUANG Feng-lei. Study on the Resistance Characteristics of Elliptical Cross-Section Projectile Penetrating Concrete. Transactions of Beijing Institute of Technology,2019,39(02):135-141.

[2]. Heng Dong, Zihao Liu, Haijun Wu, Xudong Gao, Aiguo Pi, Fenglei Huang. Study on penetration characteristics of high-speed elliptical cross-sectional projectiles into concrete. International Journal of Impact Engineering,2019,132.

[3]. Heng Dong, Haijun Wu, Zihao Liu, Xudong Gao, Aiguo Pi, Jinzhu Li, Fenglei Huang. Penetration characteristics of pyramidal projectile into concrete target. International Journal of Impact Engineering,2020,143.

[4]. YANG Xiang, WU Hai-jun, PI Ai-guo, LI Jin-zhu, HUANG Feng-lei. Fragment Velocity Distribution of Elliptical Cross-Section Killing Warhead Amajor Circumference. Transactions of Beijing Institute of Technology,2018,38(S2):178-183.

[5]. Liangliang D, Zhenduo L, Minzu L, et al. The Dispersion Rule of Fragments about the Asymmetric Casing. Shock and Vibration, 2017, 2017:1-12.

[6]. Zhiwei Guo, Guangyan Huang, Chunmei Liu, Shunshan Feng. Effect of Eccentric Initiation on the Fragment Velocity Distribution of D-Shaped Casings Filled with Explosive Charges. Propellants, Explosives, Pyrotechnics,2018,43(12).

[7]. Zhi-wei Guo, Guang-yan Huang, Wei Zhu, Shun-shan Feng. Fragment velocity distribution of D-shaped casing with multiple fragment layers. Elsevier Ltd,2019,131.

[8]. Jianguo Ning, Yan Duan, Xiangzhao Xu, Huilan Ren. Velocity characteristics of fragments from prismatic casing under internal explosive loading. International Journal of Impact Engineering,2017,109.

[9]. Marriott CO, Davey LR, Macmahon J, Fairlie GE, Ranson HJ. Computer modellin of small fragmenting warheads in 3D[C]. In: The 16th international symposium on ballistics; 1996.

[10]. Zhi-wei Guo, Guang-yan Huang, Han Liu, Shun-shan Feng. Fragment velocity distribution of the bottom part of d-shaped casings under eccentric initiation. International Journal of Impact Engineering,2020,144.

[11]. Huang GY, Li W, Feng SS. Fragment velocity distribution of cylindrical rings under eccentric point initiation. Propell Explos Pyrotech, 2015;40:215-20.

[12]. Feng ss, Jiang JW, He SL, Zhou SS. On the pattern of radial distribution pattern of initiation velocities of fragments under asymmetrical initiation. Acta Armamentarii,1993:12-6 Supplement.

[13]. Liuli Song. Study on fragment velocity distribution and enhancement regularities of eccentric priming directional warheads. Nanjing University of Science and Technology, 2008.

[14]. Shengtao Lv, Xiangdong LI, Yadong Yang. The Fragments Velocity and Destiny Distribution of the Eccentric Detonation Aimed warhead. Chin J Expl Propell, 2010, 33 (5): 79-82.

[15]. Waggener S. Relative performance of anti-air missile warheads[C]. In 19th International Symposium of Ballistic, Interlaken, Switzerland, 2001.

[16]. Yuan Li,Yuquan Wen. Experiment and numerical modeling of asymmetrically initiated hexagonal prism warhead. Advances in Mechanical Engineering,2017,9(1).

[17]. Yuan Li, Yan-hua Li, Yu-quan Wen. Radial distribution of fragment velocity of asymmetrically initiated warhead. International Journal of Impact Engineering,2017,99.

[18]. Li, Y., Li, X., Xiong, S., & Wen, Y. (2018). New Formula for Fragment Velocity in the Aiming Direction of an Asymmetrically Initiated warhead. Propellants, Explosives, Pyrotechnics, 43(5), 496-505.

[19]. Zulkoski T. Development of optimum theoretical warhead design criteria. China Lake, California, USA: Naval Weapons Center;1976. Report No NWC-TP-5892.

[20]. Xue Zaiqing, Qiao Liang, Wang Kai, et al. A preliminary study on the distribution law of the initial velocity of the fragmentation of the small cone angle elliptical killing warhead[C]//Proceedings of the 15th National Warfare and Damage Technology Academic Exchange Conference. Beijing, 2017:472-479. (in Chinese)

[21]. Yueguang Gao, Bo Zhang, Xiaomin Yan, Tong Zhou, Xiang Xiao, Shunshan Feng. Axial distribution of fragment velocities from cylindrical casing with air parts at two ends. Elsevier Ltd,2020,140.

[22]. Yusong Miao, Xiaojie Li. Munroe effect of detonation wave collision. Explosion and Shock Waves,2017,37(03):544-548.

[23]. Gilbert F. Kinney, Kenneth J. Graham. Explosive Shocks in Air, 2nd. 1962.

[24]. Li Wan. Research on the dispersion characteristics of fragments from a cylindrical casing under eccentric initiation. Beijing Institute of Technolog,2017.

[25]. An, X., Dong, Y., Liu, J., & Tian, C. (2018). General formula to calculate the fragment velocity of warheads with hollow core. International Journal of Impact Engineering, 113, 1-8.

[26]. Wei Li, Guang-yan Huang, Shun-shan Feng. Effect of eccentric edge initiation on the fragment velocity distribution of a cylindrical casing filled with charge. International Journal of Impact Engineering,2015,80: 107-15.

[27]. Huang GY, Li W, Feng SS. Axial distribution of fragment velocities from cylindrical casing under explosion loading. Int J Impact Eng 2015; 76:20-7.

[28]. Zhi-wei Guo, Guang-yan Huang, Wei Zhu, Han Liu, Shun-shan Feng. Mechanism and suppression of the effect of axial rarefaction waves on the eccentric initiation effect. Elsevier Ltd,2019,124.

[29]. Zhiwei Guo,Guangyan Huang,et al. Velocity axial distribution of fragments from non-cylindrical symmetry explosive-filled casing. International Journal of Impact Engineering, 2018, 118: 1-10.

[30]. Grisaro H, Dancygier AN. Numerical study of velocity distribution of fragments caused by explosion of a cylindrical cased charge. Int J Impact Eng, 2015;86:1–12.

[31]. Dynamics C. Release 14.0 documentation for ANSYS AUTODYN. USA: ANSYS Inc; 2011.

[32]. M BUYUK, H KURTARAN, D MARZOUGUI, et al. Automated design of threats and shields under hypervelocity impacts by using successive optimization methodology. International Journal of Impact Engineering, 2008, 35: 1449-1458.

[33]. Zhang Xianfeng. Terminal Effects. Bei Jing: BEIJING INSTITUTE OF TECHNOLOGY PRESS,2017.

[34]. Mader C.L., Numerical Modeling of Explosives and Propellants, 3rd ed., CRC Press, Florida, 2008.